Supplementary Information

Harnessing enhanced lithium-ion storage in self-assembled organic nanowires for batteries and metal-ion supercapacitors

Ievgen Obraztsov,[1*] Rostislav Langer,[2] Jean G.A. Ruthes,[4,5] Volker Presser,[4,5,6] Michal Otyepka,[1,2] Radek Zbořil,[1,3*] and Aristides Bakandritsos[1,3*]

1. Regional Centre of Advanced Technologies and Materials (RCPTM), Czech Advanced Technology and Research Institute (CATRIN), Palacký University Olomouc, Šlechtitelů 27, Olomouc, 77 900, Czech Republic
2. IT4Innovations, VŠB-Technical University of Ostrava, 17. listopadu 2172/15, 708 00 Ostrava-Poruba, Czech Republic
3. Nanotechnology Centre, Centre of Energy and Environmental Technologies, VŠB-Technical University of Ostrava, 17. listopadu 2172/15, 708 00 Ostrava-Poruba, Czech Republic
4. INM - Leibniz Institute for New Materials, Campus D2 2, 66123 Saarbrücken, Germany
5. Department of Materials Science and Engineering, Saarland University, Campus D2 2, 66123 Saarbrücken, Germany
6. saarene - Saarland Center for Energy Materials and Sustainability, Campus C4 2, 66123 Saarbrücken, Germany

* Corresponding authors.

IO: ievgen.obraztsov@upol.cz; RZ: mailto: radek.zboril@upol.cz; AB: a.bakandritsos@upol.cz

This PDF file includes:

List of abbreviations

AM	active material
CB	carbon black
CE	Coulombic efficiency
COF	covalent organic framework
CNTs	carbon nanotubes
CV	cyclic voltammetry
DFT	density functional theory
DMC	dimethyl carbonate
DSC	differential scanning calorimetry
EC	ethylene carbonate
EDS	energy-dispersive X-ray spectroscopy
EIS	electrochemical impedance spectroscopy
EM	electrode material
EMC	ethyl methyl carbonate
FEC	fluoroethylene carbonate
GITT	galvanostatic intermittent titration technique
LIB	lithium-ion battery
LIC	lithium-ion capacitor
PANI	polyaniline
PAW	projector-augmented wave
PBE	Perdew, Burke, and Ernzerhof (functional)
PHATN	perylene diimide-hexaazatrinaphthylene molecule
PVDF	polyvinylidene fluoride
NMP	*1*-methyl-*2*-pyrrolidone
MelA	mellitic acid
MA	maleic acid
MelA-C	mellitic acid:carbon black (50:50 by mass)
MelA-P	mellitic acid:carbon black:polyaniline (50:40:10 mass%)
MelA-P-NMP	mellitic acid:carbon black:polyaniline (50:40:10 mass%), prepared in NMP
MelA-P-hot	mellitic acid:carbon black:polyaniline (50:40:10 mass%), cast over hot plate
MelA-P-Ti	mellitic acid:carbon black:polyaniline (50:40:10 mass%), cast over Ti
OCP	open-circuit potential.
SEI	solid electrolyte interface
VASP	Vienna Ab-initio Simulation Package

Methods

Reagents and Materials

Mellitic acid, polyaniline (emeraldine base, average M_w ~50,000), solvents, battery-grade $LiPF_6$, and electrolyte components were purchased from Sigma-Aldrich. The 0.75 mm-thick lithium metal foil (99.9%) was from Alfa Aesar, carbon black (Imerys Super P C45) was supplied by Cambridge Energy Solutions. All reagents were used as received.

Characterization techniques

High-resolution transmission electron microscopy (HR-TEM) and scanning transmission electron microscopy (STEM) in high-angle annular dark-field (HAADF) mode for elemental mapping were performed with an FEI TITAN G2 60-300 HRTEM microscope with an X-FEG type emission gun, operating at 80 kV, objective-lens image spherical aberration corrector, and ChemiSTEM energy-dispersive X-ray spectroscopy (EDS) detector. As prepared electrode material for HR-TEM and STEM was collected from the substrate foil. Scanning electron microscopy was performed with Hitachi SU6600 with an acceleration voltage 1.5 kV. As prepared electrode material on Cu foil was used.

X-ray photoelectron spectroscopy (XPS) measurements were performed with a PHI VersaProbe II (Physical Electronics) spectrometer equipped with an Al Kα source (15 kV, 50 W). The C1s core level was set as a reference (the C-C bond, binding energy 284.8 eV) to charge-shift the spectra. The MultiPak (Ulvac-PHI, Inc.) software package was used to evaluate and deconvolute the obtained data, involving a Shirley back-ground subtraction and Gaussian-Lorentzian functions for peak fitting. As prepared electrode material was collected from the substrate foil.

Cyclic voltammetry and EIS measurements were performed using a BCS-810 system connected to an Arbin Multi-Zone Temperature Chamber (Arbin Instruments) through a custom-made adapter and VSP-3e potentiostat equipped with an EIS module (BioLogic Science Instruments). Charge-discharge rate and stability tests were performed using Novonix UHPC system with a dedicated thermostatic chamber (Novonix). Electronic conductivity of materials was measured with the four-point probe (Ossila).

Electrode preparations

The pure MelA anode was prepared by drop-casting water solution of MelA onto a Cu current collector coins, followed by drying at room temperature for one hour and overnight in a vacuum oven at +100 °C. MelA-P (MelA:CB:PANI, 50:40:10 by mass) electrodes were prepared by dissolving mellitic acid in ultrapure water (18 MΩ), dispersing polyaniline (emeraldine base) in this solution by ultrasonication for 24 h, and mixing the dispersion with a carbon black powder (Imerys SuperP C45) in a Thinky ARV-310 planetary mixer (Thinky Co.) for 5 min at 1100 rpm under pressure decreased to 30 kPa. The specific ratio for MelA: CB: PANI: water in MelA-P is 1: 0.8: 0.2 : 12.5 by mass (MelA: CB: PANI, 50:40:10 mass%). The slurry was cast onto a 10-µm thick copper foil (Cambridge Energy Solutions) with a 100-µm slot of doctor blade. The mass loading and thickness were 0.8–1.0 mg cm^{-2} and 28–34 µm, respectively. Films were dried at room temperature for 30 min and overnight in a vacuum oven at 100 ℃. Dry films were cut into 15-mm disks, weighed, and stored in an Ar-filled glove box ([O_2] and [H_2O] < 0.8 ppm) before use. The MelA-C (MelA:CB, 50:50 by mass) electrodes were prepared following the above-described procedure without ultrasonication. The specific ratio for MelA: CB: water in MelA-C is 1: 1: 17.5 by mass, respectively (MelA:CB, 50:50 mass%). The mass loading of the electrode material was 0.8–1.0 mg cm^{-2}, and the film thickness of 20–24 µm.

Slurry preparation with other carbon additives was not successful because only Imerys Super P C45 was forming a uniform aqueous dispersion. Lower contents of CB than 50 mass% also did not lead to stable films.

The CB and PANI electrodes for determination of their individual contribution to the capacity of the MelA-P anode were prepared by planetary mixing with PVDF in NMP (5 min at 1100 rpm., under pressure decreased to 30 kPa) in the 70:30 ratio by mass.

The PC cathode was prepared by mixing PC (ACS Materials) with CB (Ketjenblack EC-600JD, AkzoNobel Functional Chemicals BV) and PVDF (Merk) in the 90:3:7 (by mass) ratio in *1*-methyl-*2*-pyrrolidone (NMP). The planetary-mixed slurry was cast over carbon-coated Al foil (Cambridge Energy Solutions, thickness 15 µm) and dried in a vacuum oven at +120 °C overnight. The film was calendered between steel plates compressed with the 4 kN cm^{-2} pressure.

The graphite and terephthalic electrodes for DSC measurements were prepared by mixing active materials with carbon black (SuperP C45, Imerys) and PVDF in the 92:2:6 and 50:40:10 ratio, respectively, in NMP.

In Supplementary Table 2 all the samples that were prepared in this work for the main study or for comparison are listed.

Cell assembling

The CR2032 and research-grade coin cells (PAT-cell of EL-Cell GmbH) were assembled using lithium metal coin (15.5 mm diameter, 0.75 mm thickness), Whatman GF/A separator, and 1.0 M $LiPF_6$ EC:DMC:EMC (ethylene carbonate:dimethyl carbonate ethyl methyl carbonate 1:1:1 by mass) with 10 vol% of FEC (fluoroethylene carbonate) as the counter/reference electrode, separator, and electrolyte (100 µL), respectively. The lithium metal surface was mechanically refreshed before cell assembling.

LIC preparation and cell assembly. MelA-P anode was precycled with three charge-discharge cycles at 0.05 A g^{-1} and ten charge-discharge cycles at 0.2 A g^{-1} to activate the electrode material and stabilize its capacity. The anode was lithiated to 0.01 V vs. Li^+/Li before cell assembling. The PC cathode was calendared, verified by current rate performance in the 2.0–4.5 V potential range vs Li. The C:A mass ratio was 1:3.8.

Electrochemical performance tests

All cells were kept at OCP for 6 h before measurements, and experiments were performed at +25 °C ± 0.2°C unless other specified. All specific current values in half cells correspond to the total mass of electrode material.

Mellitic acid anodes were tested in the 3.0–0.01 V vs. Li^+/Li range. The mass of all electrode components was used for capacity calculation unless otherwise specified.

The LIC rate test was performed in the 2.0–4.5 V and 1.0–4.5 V cell voltage range with 0.1 A g^{-1} to 10 A g^{-1} currents followed by 3000-cycle stability test in the cell voltage range of 2.0-4.5V. All specific current values correspond to the total mass of electrode materials of both anode and cathode. The specific energy and specific power were calculated using the mass of all electrode material components on both anode and cathode using the following equations:

$$E = \int_{t_1}^{t_2} IV dt \quad (\text{Wh kg}^{-1}) \tag{1}$$

$$P = E/t \ (\text{W kg}^{-1}) \tag{2}$$

where *I* is the specific current based on mass of all components of electrode materials on both anode and cathode, *V* is voltage of the LIC during its discharge, *t* is discharge time (s). EIS measurements were performed in a two-electrode setup in a potentiostatic mode using 10 mV AV oscillation amplitude over the frequency range of 0.1 Hz to 10 kHz after 1 h of equilibration at the open-circuit potential.

Computational Methods

The periodic calculations were executed by spin-polarized Density functional theory (DFT) in a Vienna Ab-initio Simulation Package (VASP). [1,2,3] The electron-ion interactions were treated by a projector-augmented wave (PAW) method,[4,5] and the Perdew, Burke, and Ernzerhof (PBE) functional[6] and empirical Grimme D2 dispersion.[7] The basis set contained plane waves with a maximum kinetic energy of 400 eV and a Γ-centered 6 × 6 × 1 *k*-point mesh. All structures were optimized until the forces acting on all atoms were reduced to less than 10 meVÅ^{-1}, and the electronic and magnetic degrees of freedom were relaxed until the change in total energy between the successive iteration steps was smaller than 10^{-5} eV.
The binding energy, E_b, per lithium atom was evaluated as

$$E_b = 1/n(E_{MelA+Li} - E_{MelA-Li} - nE_{Li}) \quad (3)$$

where $E_{MelA+Li}$, $E_{MelA-Li}$ and E_{Li} stands for total energies of the whole mellitic acid-lithium system, and mellitic acid system without Li and lithium atoms, respectively, *n* denotes the number of lithium atoms.

Differential scanning calorimetry measurements

For the DSC measurement, three electrodes were prepared: graphite (graphite: CB: PVDF, 92:2:6) as the most common anode material for lithium storage, terephthalic acid, and MelA-P anode of identical composition (AM:CB:PANI, 50:40:10). Half-cells with these electrodes were assembled and cycled ten times followed by lithiation to 0.01 V. The lithiated cells were disassembled inside the Ar-filled glovebox, where the electrode materials were capsulated into aluminum pans without washing off the electrolyte. The DSC measurements were performed using hermetically capsulated materials heated to +220 °C at the 10 °C min^{-1} (Supplementary Fig. 22).

Supplementary Note 1

The specific capacity of mellitic acid in electrode materials was calculated using the following equations:

$$Q_{MelA} \text{ (in MelA-C)} = w_{MelA}\, Q_{MelA} + w_{CB}\, Q_{CB} = Q_{EM} - w_{CB}\, Q_{CB} \quad (4)$$

$$Q_{MelA} \text{ (in MelA-P)} = w_{MelA}\, Q_{MelA} + w_{CB}\, Q_{CB} + w_{PANI}\, Q_{PANI} \quad (5)$$

$$Q_{100\%\ CB} \text{ (in CB:PVDF, 70:30 by mass)} = 1.43\, Q_{EM\ measured} \quad (6)$$

Assuming zero capacity of PVDF:

$$Q_{100\%\ MelA} = \frac{Q_{EM\ measured} - (\omega_{CB} \times Q_{100\%\ CB})}{\omega_{MelA}} \quad (7)$$

assuming zero capacity of PANI in the 0.01-3.0 V vs Li^+/Li potential range, because PANI:CB composition has lower capacity than CB:PVDF (Supplementary Figs. 9,10).

Supplementary Note 2

The maximal redox-specific capacity of an organic active material can be calculated using the equation:

$$Q_{theor} = \frac{nF\ (C\ mol^{-1})}{M_r\ (g\ \ mol^{-1})} = \frac{n \times 96485\ (C)}{M_r\ (g)} = \frac{n \times 96485\ (A\ s)}{M_r\ (g)} = \frac{n \times 96485 \times 1000/3600\ (mA\ h)}{M_r\ (g)} \quad (8)$$

where n is the number of electrons transferred or single-valence cations bound per molecule.

Assuming reversible binding of a maximum of 6 Li^+ by a single MelA molecule, the maximal theoretical specific capacity is:

$$Q_{MelA,\ max} = \frac{6 * 26801}{342.16} = 470\ mAh\ g^{-1} \quad (9)$$

Supplementary Note 3

For qualitative evaluation of kinetic processes in the nanorod MelA-P anode power law analysis was performed to determine the nature of electrochemical processes during the charge and discharge of the anode.[8] The b-value from the equation $i_p = av^b$ was determined (Fig. 4b) from the slope of the log-log plot of current (i) versus the scan rate (v) at different potentials. The limiting values 0.5 and 1.0 of this parameter reflect the occurrence of a pure diffusion- or surface-controlled process.[8] The intermediate b-values in most of the observed potential range indicate mixed diffusion-limited and surface-controlled energy storage mechanisms.

The contribution of the diffusion- and surface-controlled current in the overall current response during cyclic voltammetry was evaluated by k_1-k_2 analysis using equation $i = k_1v + k_2v^{1/2}$. Here, the k_1v and $k_2v^{1/2}$ are the surface-controlled and diffusion-controlled components of the total current, v is the potential scan rate, and k_1 and k_2 are potential sweep-rate independent constants.[8] The k_1 and k_2 for fixed potentials were determined from the slope and y-axis intercept point of the $i/v^{1/2}$ versus $v^{1/2}$ plot.

Supplementary Note 4

GITT measurements were performed in a CR2032 coin cell with MelA-P anode vs. Li metal after a rate test. The GITT program consisted of 30 min/0.1 A g^{-1} current pulses followed by 120 min relaxation at open-circuit potential. The diffusion coefficient was calculated according to the equation derived by Weppner and Huggins,[9] simplified for small currents (Ref. [10]):

$$D_{Li+} = \frac{4}{\pi\tau}\left(\frac{n_M V_M}{M_r S}\right)^2\left(\frac{\Delta E_s}{\Delta E_t}\right)^2 \tag{10}$$

where D_{Li^+} ($cm^2\ s^{-1}$) is the Li^+ apparent diffusion coefficient, t is the duration of the current pulse (s), n_M and V_M are the mass (mol) and molar volume ($cm^3\ mol^{-1}$), respectively. The M_r and S are the atomic weight and the interfacial area of the active material (cm^2). The ΔE_t is the change in potential corrected by ohmic potential drop, and ΔE_s is the difference in OCP measured at the end of two sequential open-circuit relaxation steps. The $\frac{m V_M}{M S}$ part of this equation is the diffusion length. Therefore, this equation can be rewritten as (Ref. [9]):

$$D_{Li+} = \frac{4 L^2}{\pi\tau}\left(\frac{\Delta E_s}{\Delta E_t}\right)^2 \tag{11}$$

where L is the average radius of nanowires (cm) determined as 32 nm from scanning electron micrographs raph seen in Supplementary Fig. 1b.

Supplementary Note 5

Normalization of specific energy and specific power to the total mass of electrode materials of both electrodes for Fig. 6d and Supplementary Table 3.

$$E_{sp\ EM} = E_{sp\ based\ on\ AM\ total} \times k \tag{12}$$

$$P_{sp\ EM} = P_{sp\ based\ on\ AM\ total} \times k \tag{13}$$

$$k = \frac{(Anode\ EM\ mass\ loading\ \times\ \omega\ anode\ AM)\ +\ (Cathode\ EM\ mass\ loading\ \times\ \omega\ cathode\ AM)}{Summ\ of\ EM\ mass\ loadings\ on\ anode\ and\ cathode} \tag{14}$$

where w is the mass fraction of an active material in the electrode material.

Supplementary Information: additional figures and tables

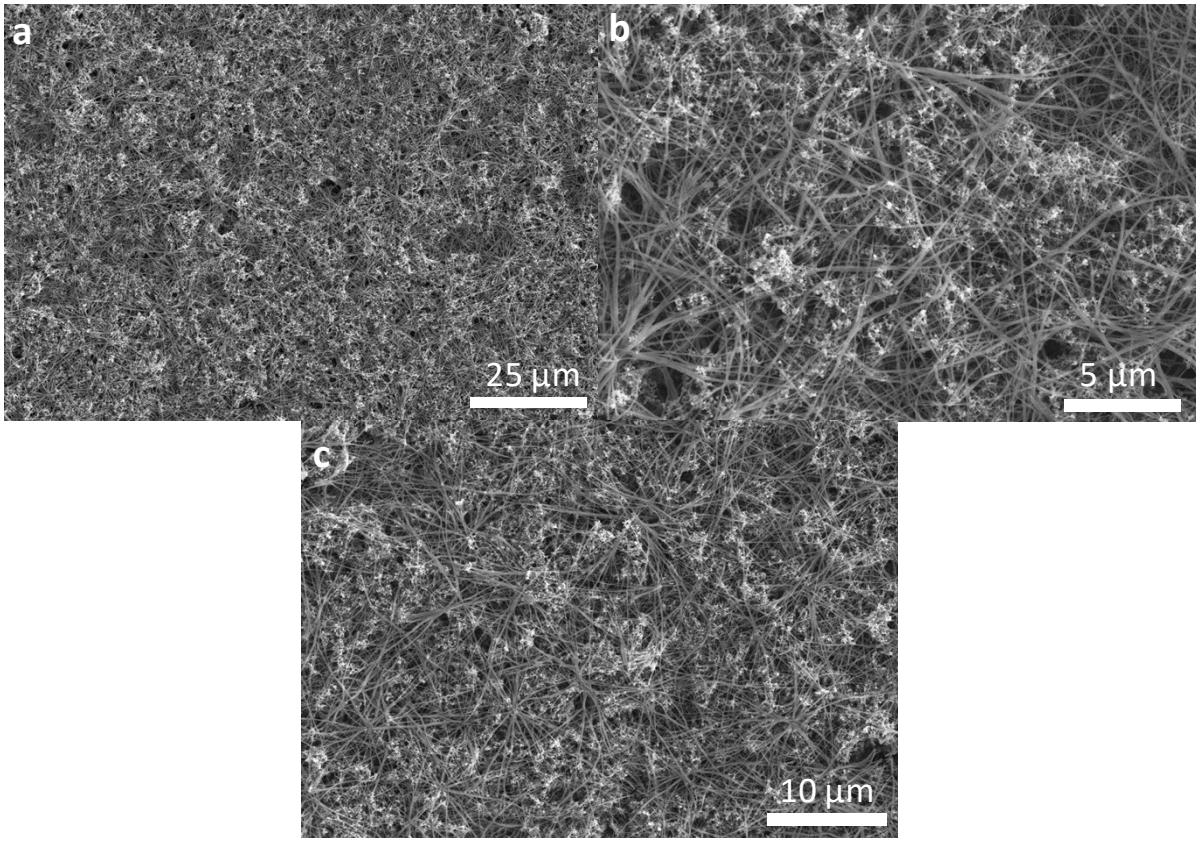

Fig. 1. Scanning electron micrographs of the (a,b) MelA-P and (c) MelA-C anodes.

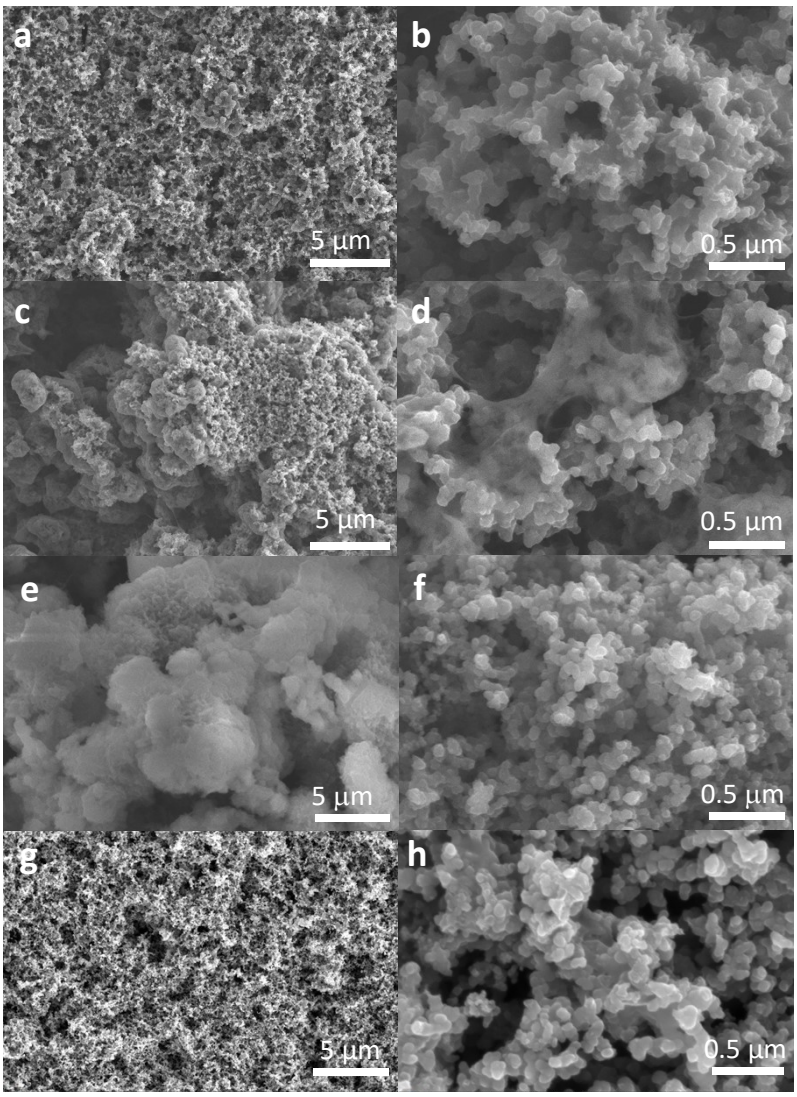

Fig. 2. Scanning electron micrographs of MelA electrodes prepared by (a, b) fast drying of the aqueous MelA-P slurry at 60 °C after casting it on the Cu current collector (MelA-P-hot, m_{EM} = 0.6 mg cm^{-2}), (c, d) drying of the MelA-P slurry by casting it on the Cu current collector at room temperature but using *1*-methyl-*2*-pyrrolidone as solvent instead of water (MelA-P-NMP, m_{EM} = 1.3 mg cm^{-2}). The scanning electron micrographs of (e) PANI, and (f) CB powder are provided here for comparison. (g,h) drying the aqueous MelA-P slurry by casting it on the Ti current collector at room temperature (MelA-P-Ti).

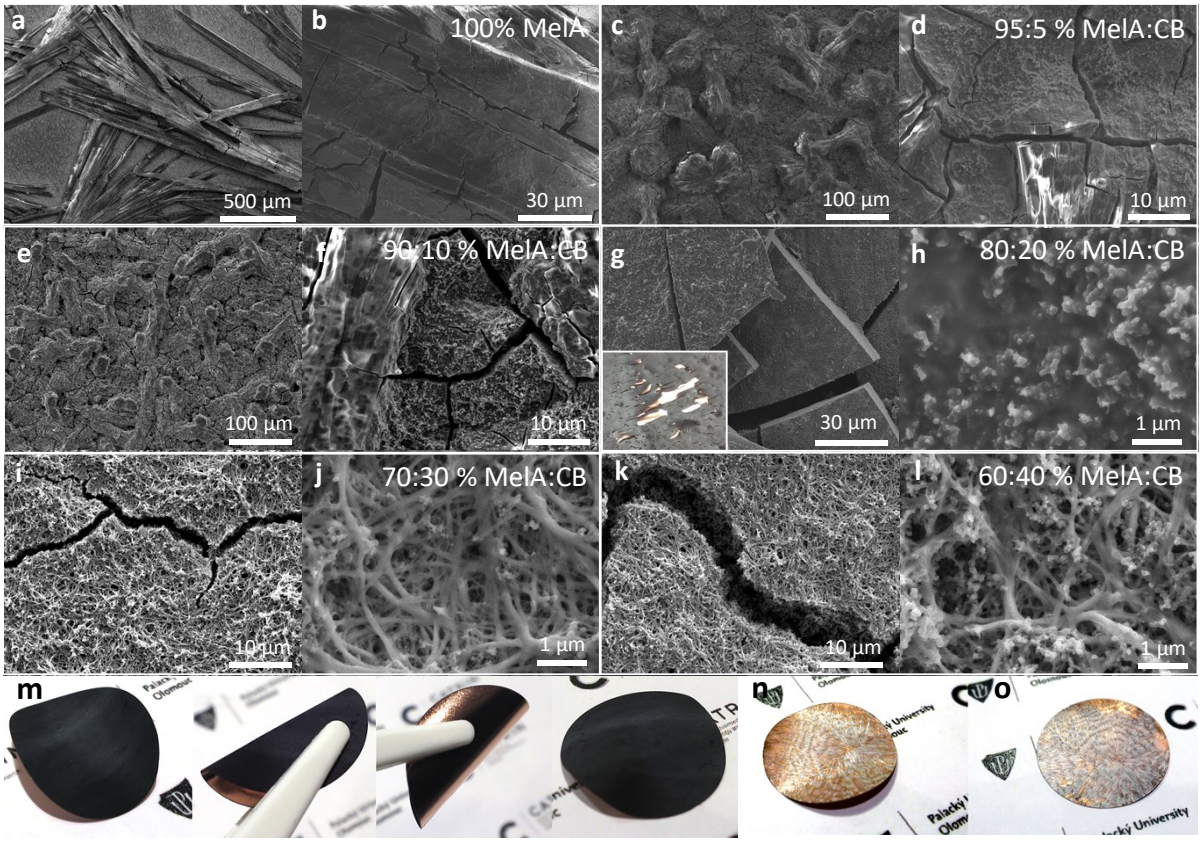

Fig. 3. Scanning electron micrographs of the (a,b) pure MelA on copper substrate, and MelA:CB films with different mass ratios: (c,d) 95:5 %, (e,f) 90:10 %, (g,h) 80:20 %, (i,j) 70:30 %, (k,l) 60:40 %. Insert in the panel "g" shows a photograph of cracked and peeled off film. Photographs (m) before, during, and after mechanical bending of MelA-nanowire anode on the Cu current collector, (n) pure MelA deposited onto copper collector before and (o) after 40-cycle current-rate test followed by six-week storage in the cell.

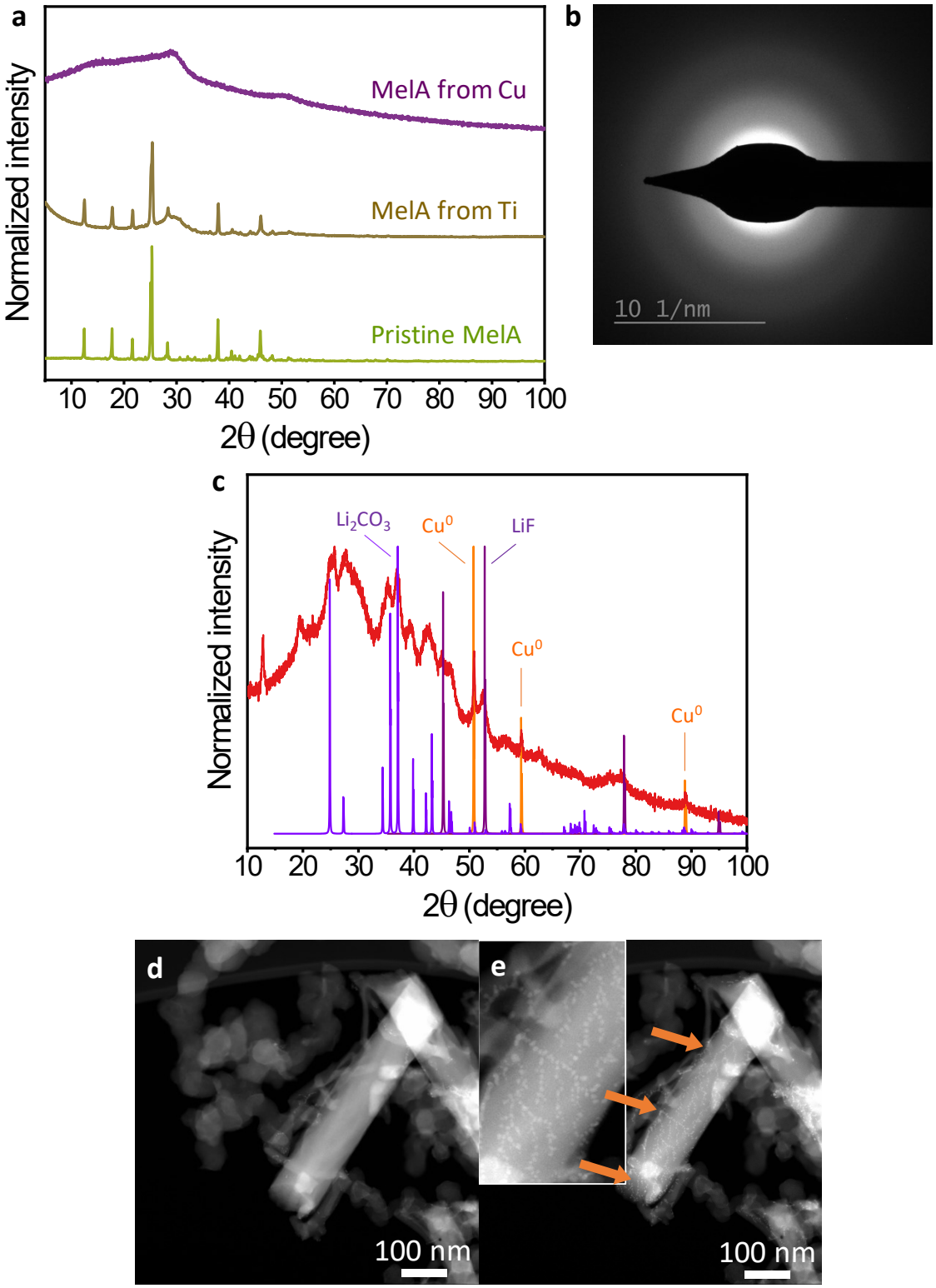

Fig. 4. (a) Normalized X-ray diffractograms from pristine MelA powder, and MelA electrode materials collected from Ti, and from Cu current collectors, and (b) selected area electron diffraction (SAED) pattern of MelA electrode material showing the amorphous nature, (c) XRD for the MelA-P electrode material after cycling, as well as reference patterns for Cu^0, LiF, and Li_2CO_3; (d) HAADF-STEM of a not cycled MelA-nanowire, (e) arrows indicate Cu^0 metal clusters reduced upon exposure of the MelA-P material to the electron beam. Inset shows magnified a MelA nanowire with Cu metal clusters.

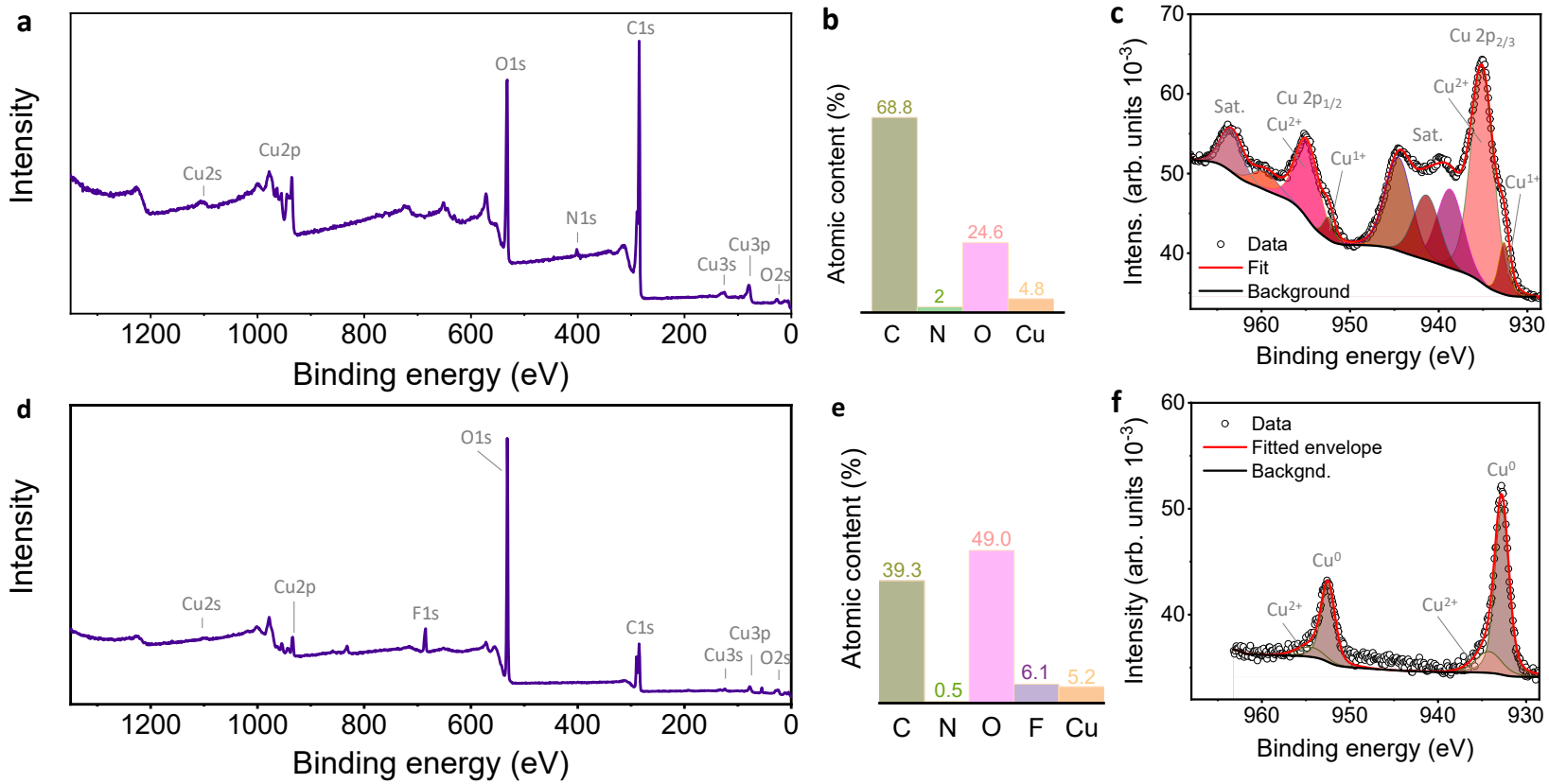

Fig. 5. Survey XPS spectrum, elements atomic contents as determined by XPS, and high-resolution XPS spectrum of Cu 2p region for the (a–c) as prepared MelA nanowire materials and (d–f) after ca. 110 h of operation. The presence of satellite peaks in panel (c) suggests that Cu^{1+} is present rather than Cu^{0}; Cu^{1+} is also suggested due to the absence of strong reducing conditions in the fresh electrode. In panel (f), the absence of satellite peaks and the clear reflections from XRD (Supplementary Fig. 4c) suggest the presence of Cu^{0}.

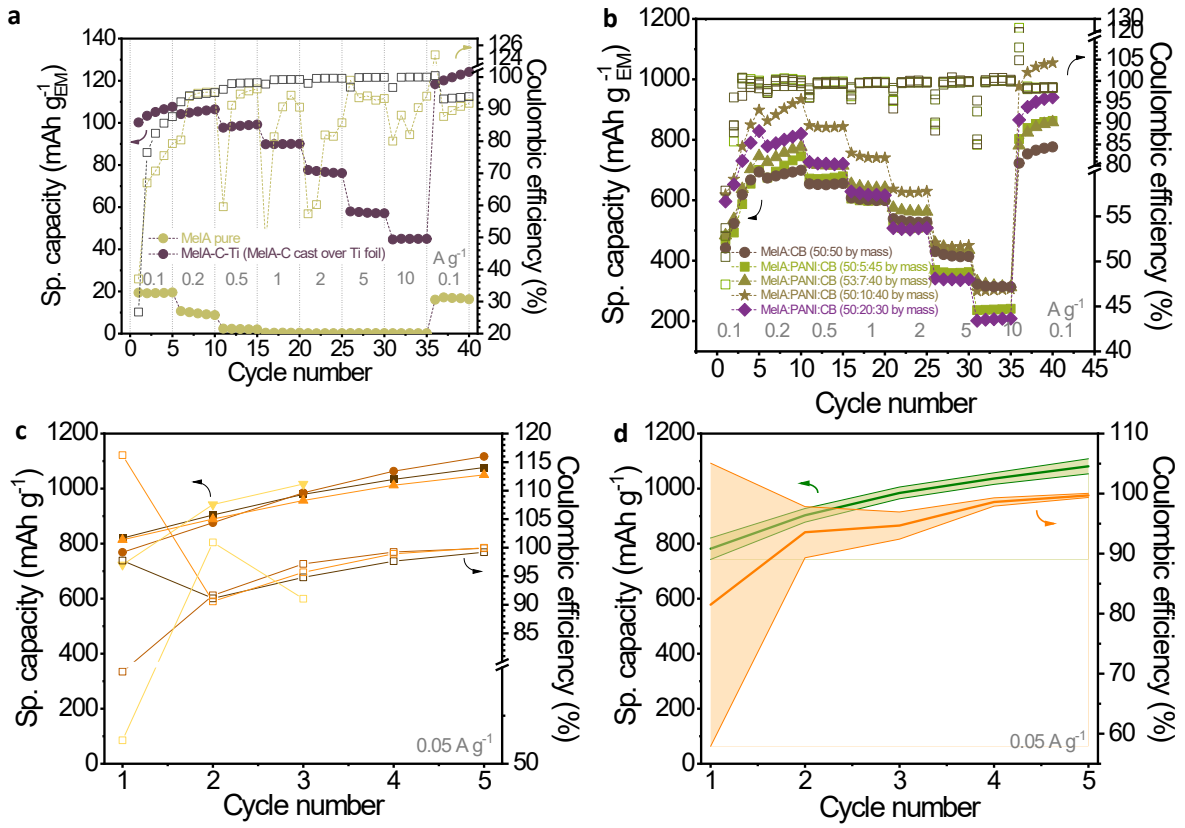

Fig. 6. Electrochemical test of (a) pristine MelA anode after drop cast on Cu current collector and MelA-P cast on pure Ti substrate (MelA-P-Ti), (b) MelA anodes of different compositions, (c) reproducibility of initial charge-discharge cycles for MelA:PANI:CB (50:10:40 by mass) at 0.05 A g^{-1} in an EM | Li half-cell, and (d) average capacity and Coulombic efficiency with standard deviation for the data in the panel c. The m_{EM} was ~1 mg cm^{-2}. Filled symbols in panels a and b represent delithiation capacity.

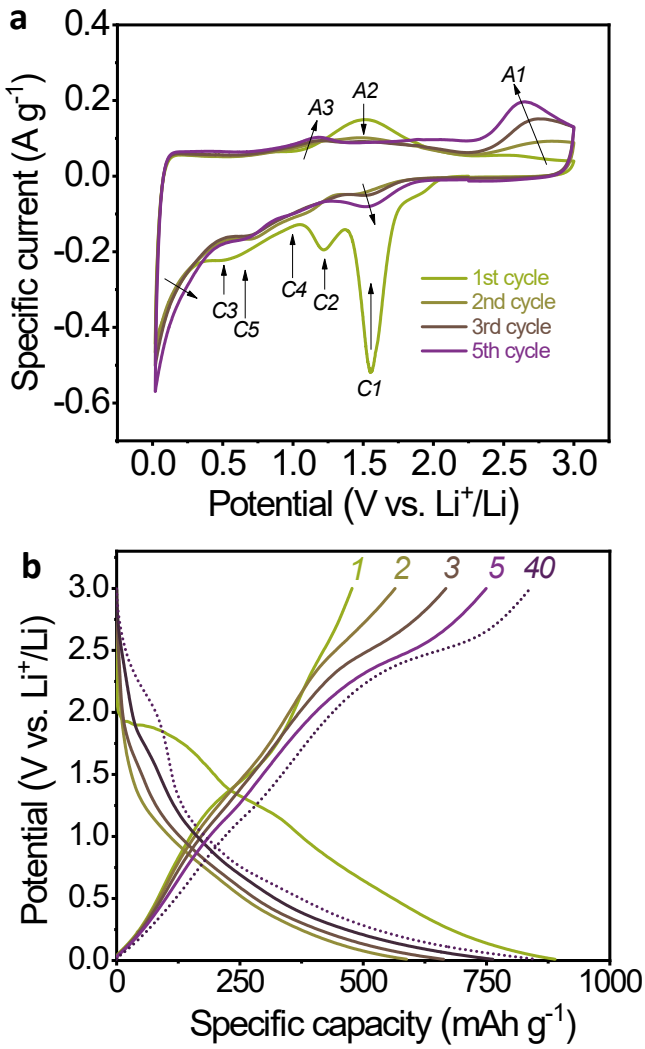

Fig. 7. Initial (a) cyclic voltammograms at 0.1 mV s^{-1} potential sweep rate, and (b) initial charge-discharge cycles at 0.1 A g^{-1} specific current for a MelA-C anode in a MelA-C|Li half-cell.

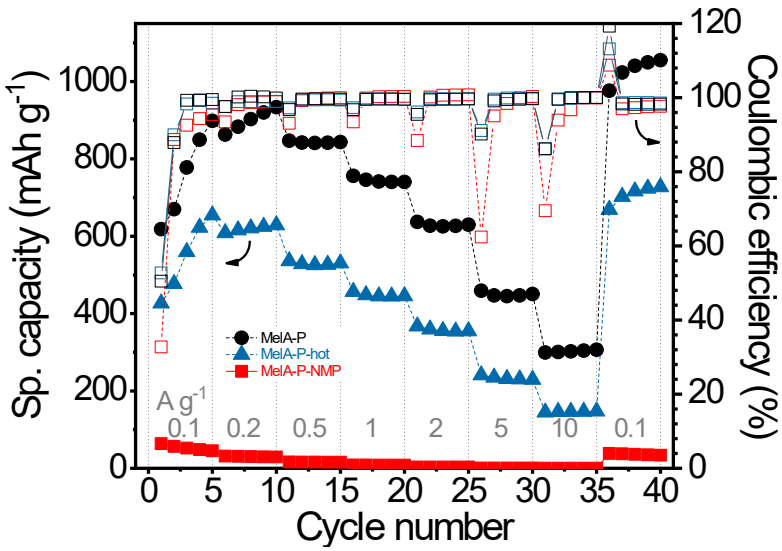

Fig. 8. Current-rate performance of MelA anodes of the same composition but different morphologies: MelA-P nanorod anode (m_{EM} = 0.8 mg cm^{-2}), MelA-P-hot - aqueous slurry cast over hot plate (m_{EM} = 0.8 mg cm^{-2}), and MelA-P-NMP – NMP-based slurry (m_{EM} = 1.3 mg cm^{-2}). Filled symbols represent delithiation capacity.

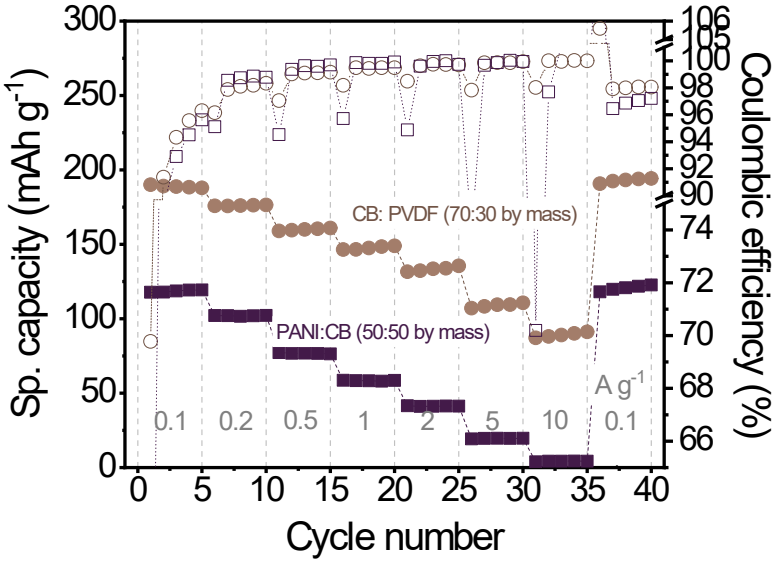

Fig. 9. Electrochemical rate capability test of carbon black (CB:PVDF, 70:30 by mass) and polyaniline (PANI:CB, 50:50 by mass) in an EM | Li half-cell. The m_{EM} was 0.53 mg cm^{-2}, and 0.66 mg cm^{-2}, respectively. Filled symbols represent delithiation capacity.

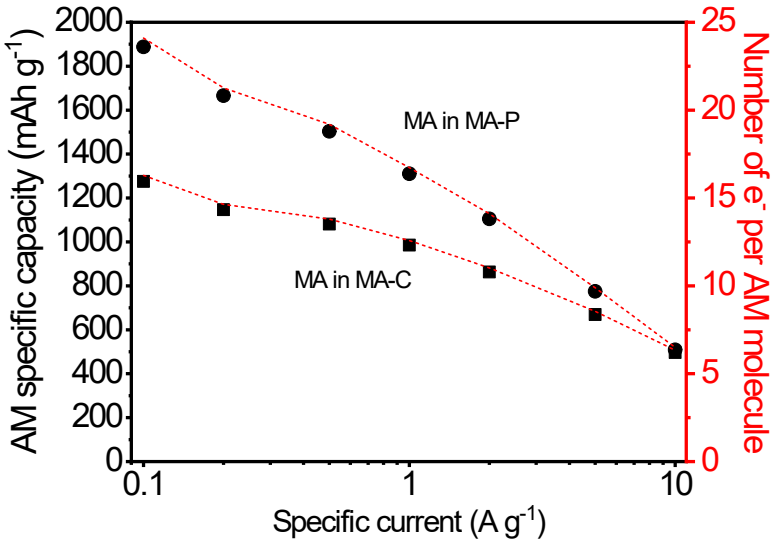

Fig. 10. The determined specific capacity of MelA and the corresponding number of Li cations bound by a single molecule; related to Supplementary Note 1 and Note 2.

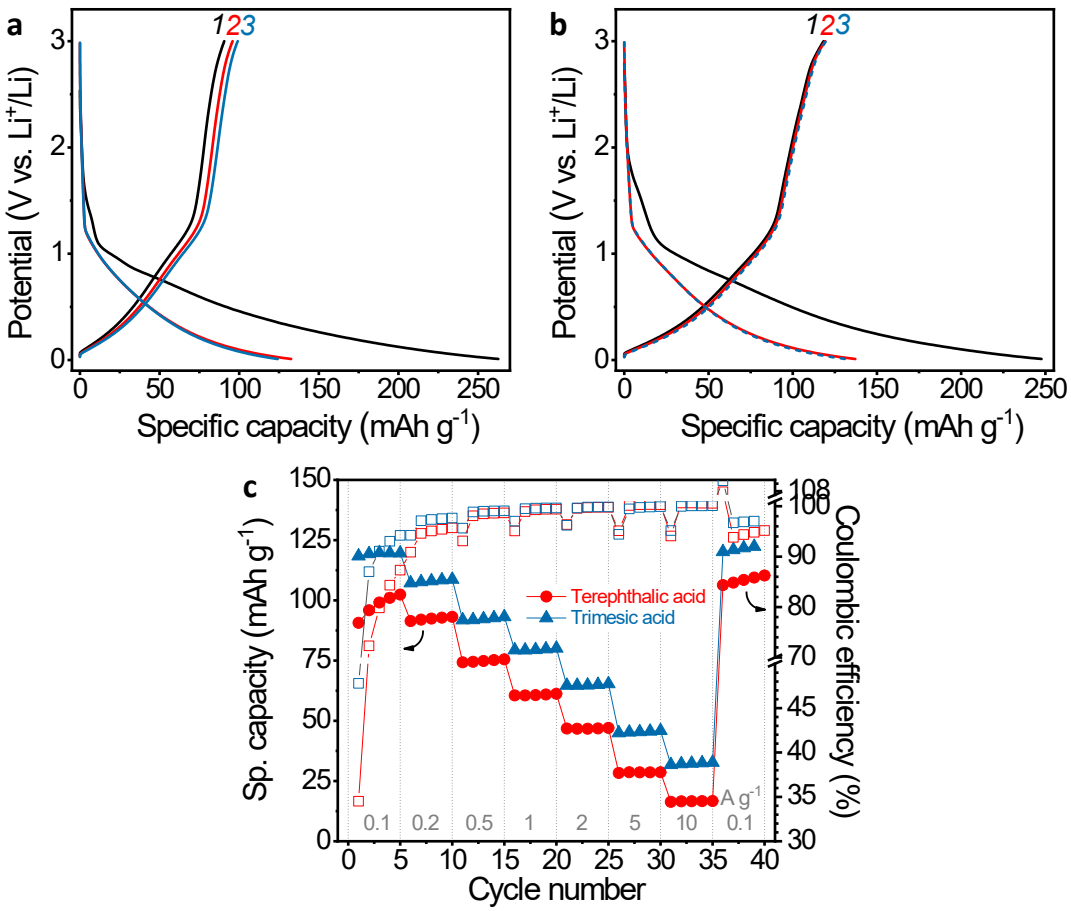

Fig. 11. Initial charge-discharge cycles for (a) terephthalic acid and (b) trimesic acid anodes (active material: CB: PANI, 50: 40: 10 by mass) at 0.1 A g^{-1}, and (c) current rate test in a EM | Li half-cell. The m_{EM} was 1.58 mg cm^{-2} and 0.88 mg cm^{-2}, respectively. Filled symbols in panel c represent delithiation capacity.

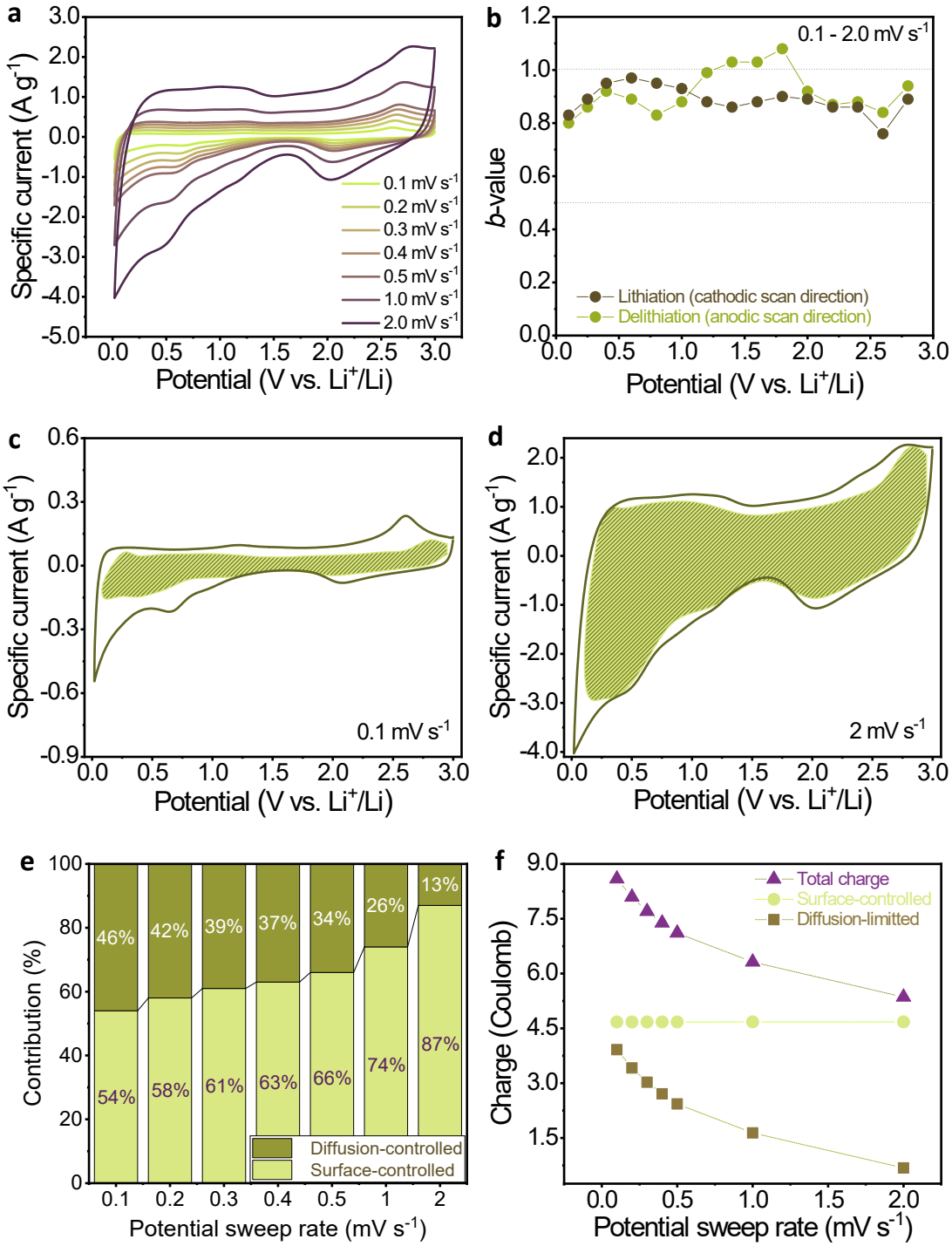

Fig. 12. (a) Cyclic voltammograms for MelA-P at different scan rates performed after the current rate test shown in the Fig. 3a, (b) *b*-values determined at different potentials, (c–d) surface-controlled fraction of charge (patterned area) in cyclic voltammograms at different potential sweep rates, (e) contribution of diffusion- and surface-controlled processes in the charge stored by MelA-P anode at different potential sweep rates, and (f) diffusion-limited, surface-controlled, and total charge values in voltammograms for MelA-P anode at different potential sweep rates.

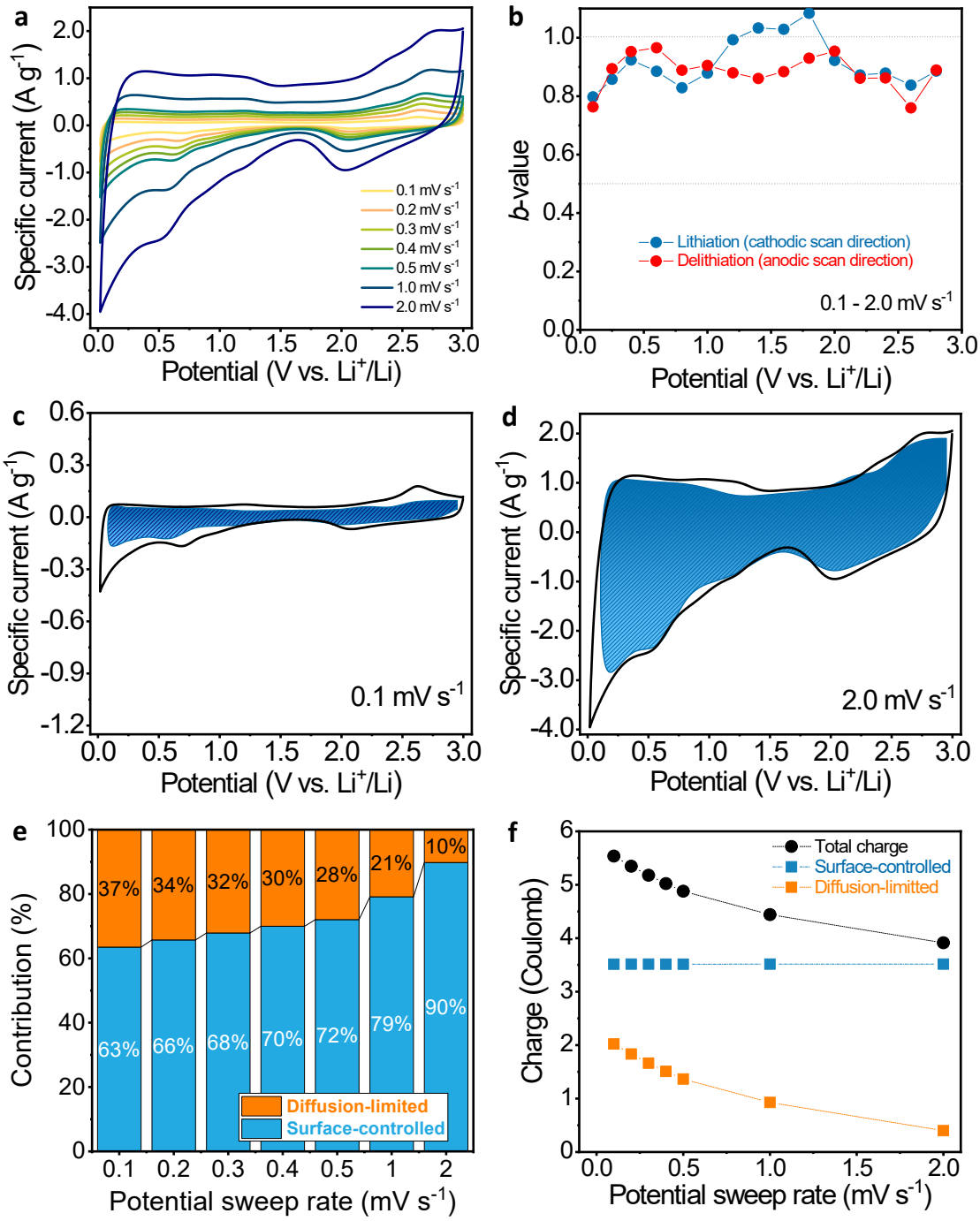

Fig. 13. (a) Cyclic voltammograms for MelA-P at different scan rates performed after the current rate test shown in the SI Fig. 6b, (b) *b*-value determined at different potentials during lithiation and delithiation of the anode, determined fraction of surface capacity-originated current (patterned area) at (c) 0.1 mV s^{-1} and (d) 2.0 mV s^{-1} potential scan rate, (e) relative contribution of diffusion-limited and surface-controlled processes to the capacity of the MelA-C anode at different potential sweep rates and (f) their numerical change. The cyclic voltammograms were recorded after the rate testing and high-rate stability test of the MelA-C anode.

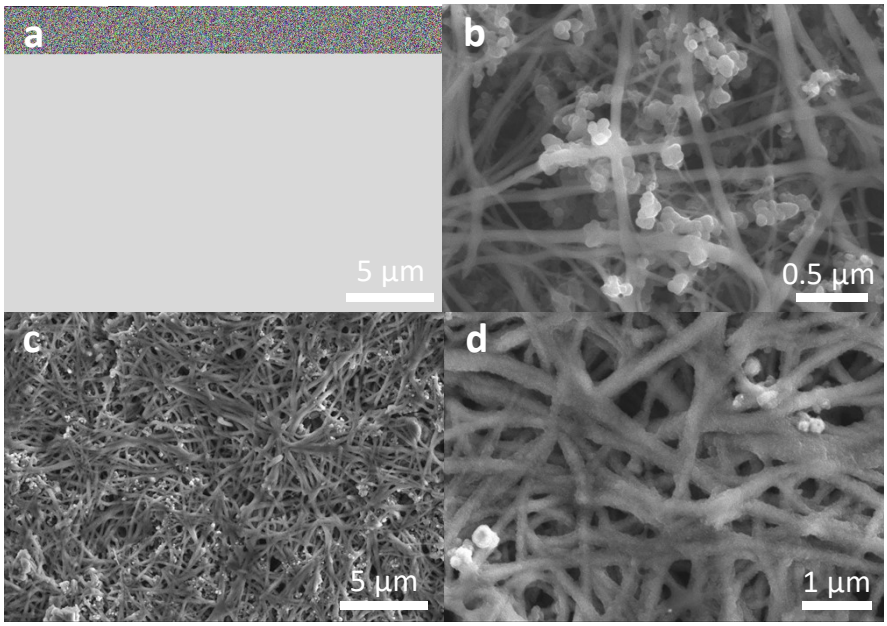

Fig. 14. Scanning electron micrographs of (a,b) the as prepared MelA-P electrode and (c,d) MelA-P electrode after 115 h of operation in a half-cell vs Li metal (3 cycles at 0.05 A g^{-1}).

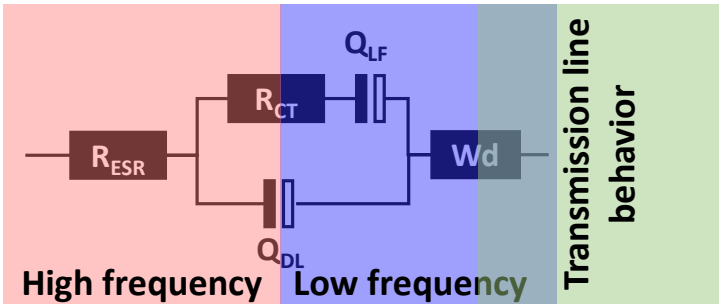

Fig. 15. Equivalent circuit used for fitting of impedance spectra. Here R_s is a bulk resistance of the cell, denoting the combined resistance of the electrolyte, separator, and electrodes, R_{CT} – charge-transfer resistance, Q_{DL} and Q_{LF} – constant phase elements describing non-ideal behavior of the tested material, W_d – the Warburg-element-related to diffusion of lithium ions on the electrode|electrolyte interface.

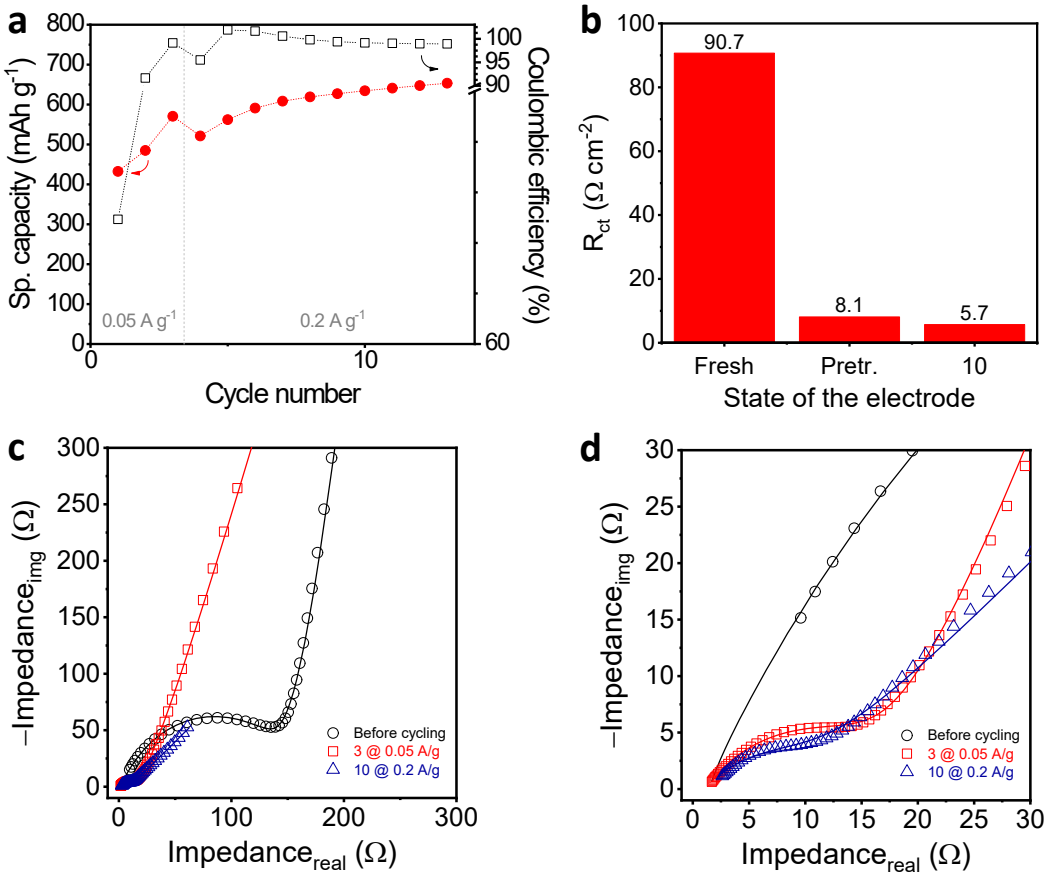

Fig. 16. (a) MelA-P-hot (nanospheres) three-cycle pretreatment at 0.05 A g^{-1} and cycling at 0.2 A g^{-1}, (b) R_{ct} for the electrode after a different number of cycles obtained from the (c) EIS recorded for a fresh electrode before cycling, after the three-cycle pretreatment at 0.05 A g^{-1}, and after 10 cycles at 0.2 A g^{-1}, and (d) magnified panel c.

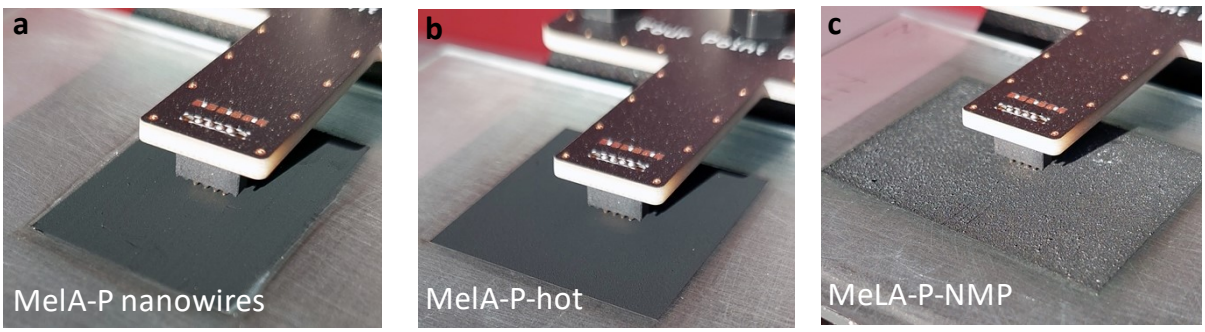

Fig. 17. Conductivity measurements of (a) MelA-P prepared by casting aqueous slurry on a glass substrate and drying at slow rate, (b) identical film cast on the substrate heated to 60 °C, and (c) MelA-P-NMP, deposited from NMP slurry (microchunks).

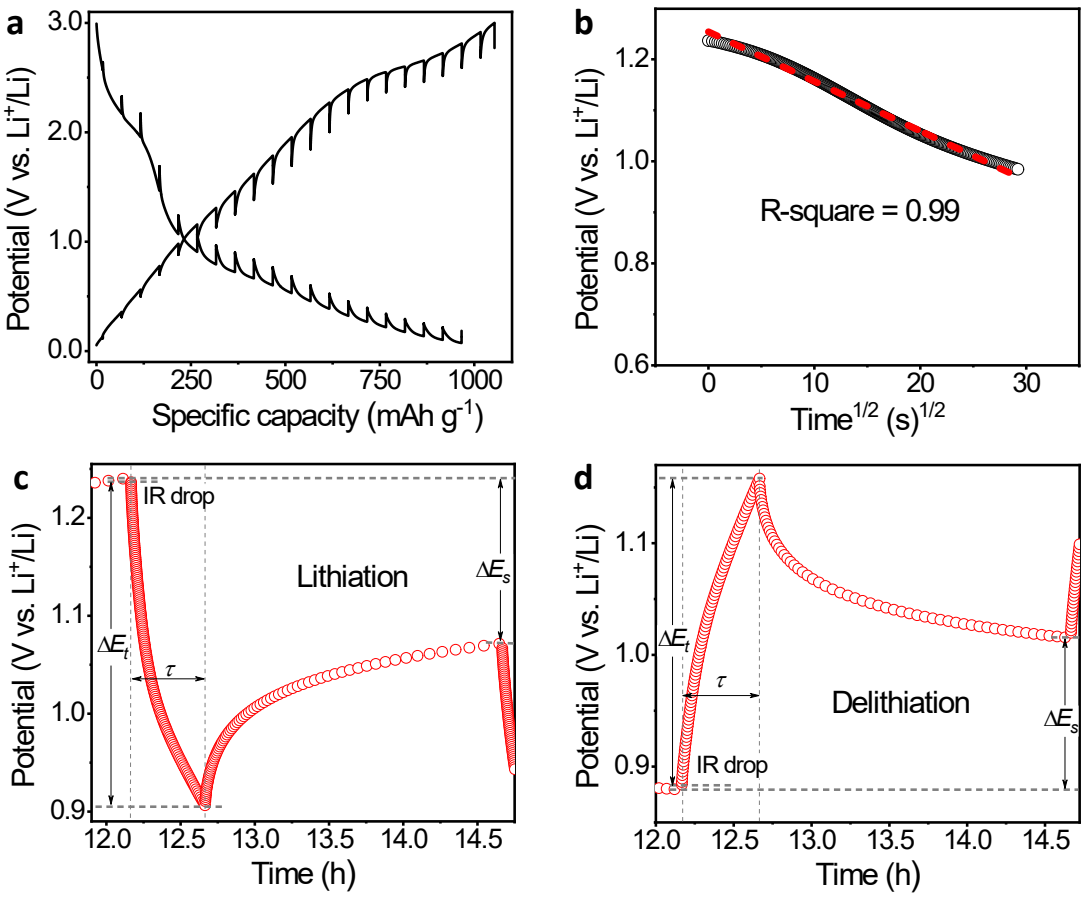

Fig. 18. Galvanostatic intermittent titration technique (a) voltage-specific capacity profiles, (b) linear fitting of potential vs. square root of time during charge pulse, (c, d) typical GITT step during lithiation and delithiation of the electrode, respectively.

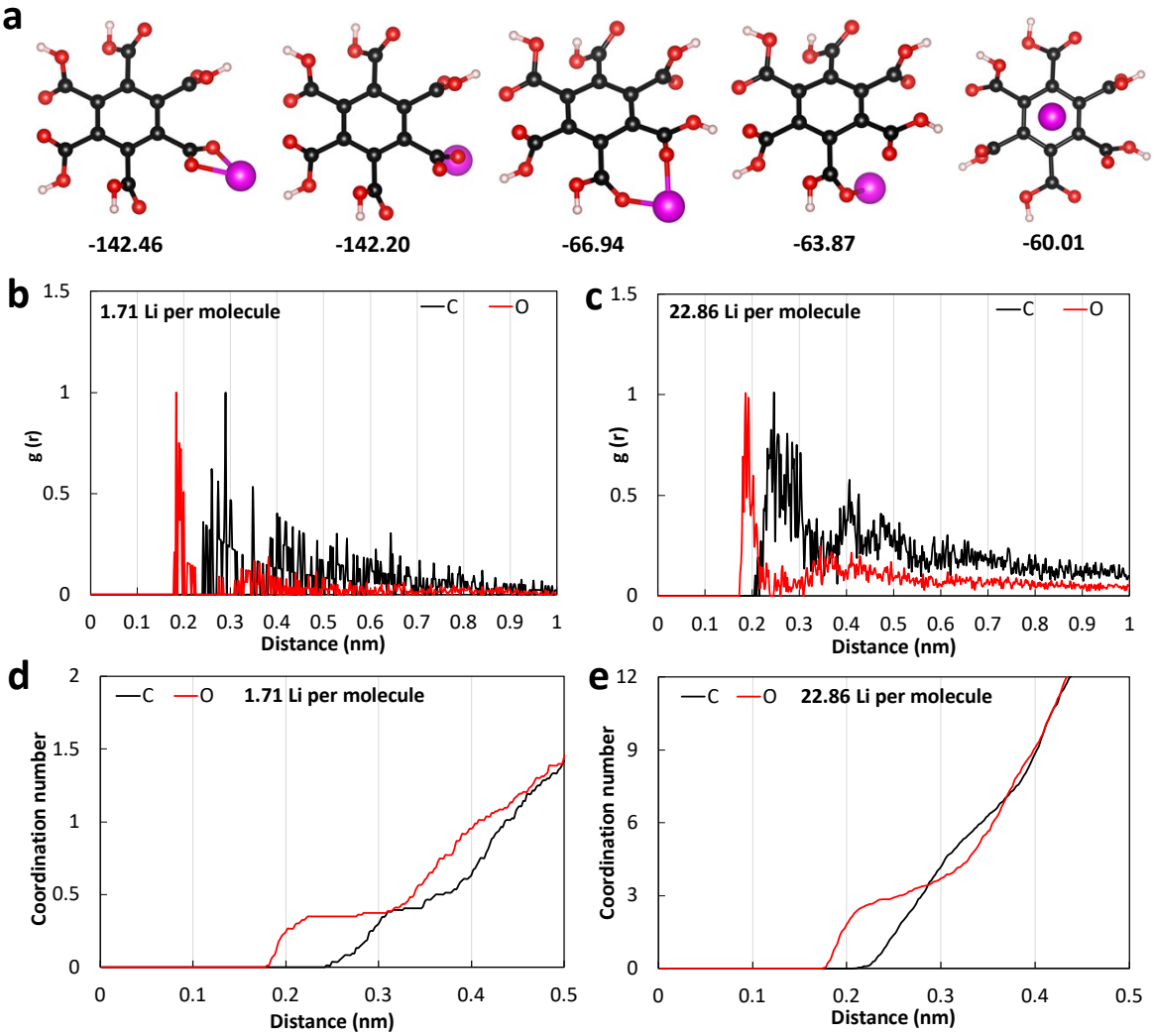

Fig. 19. (a) Finite model of a mellitic acid molecule interacting with a lithium atom. The numbers indicate the binding energies per Li atom in kcal mol^{-1}. Carbon in black, oxygen in red, hydrogen in white, lithium in magenta; (b,c) radial distribution function, g(r), of Li atoms to C and O atoms of mellitic acid calculated at (b) lower and (c) higher Li loading; (d,e) coordination number of Li around oxygen and carbon atoms as a function of distance at (d) lower and (e) higher Li loading.

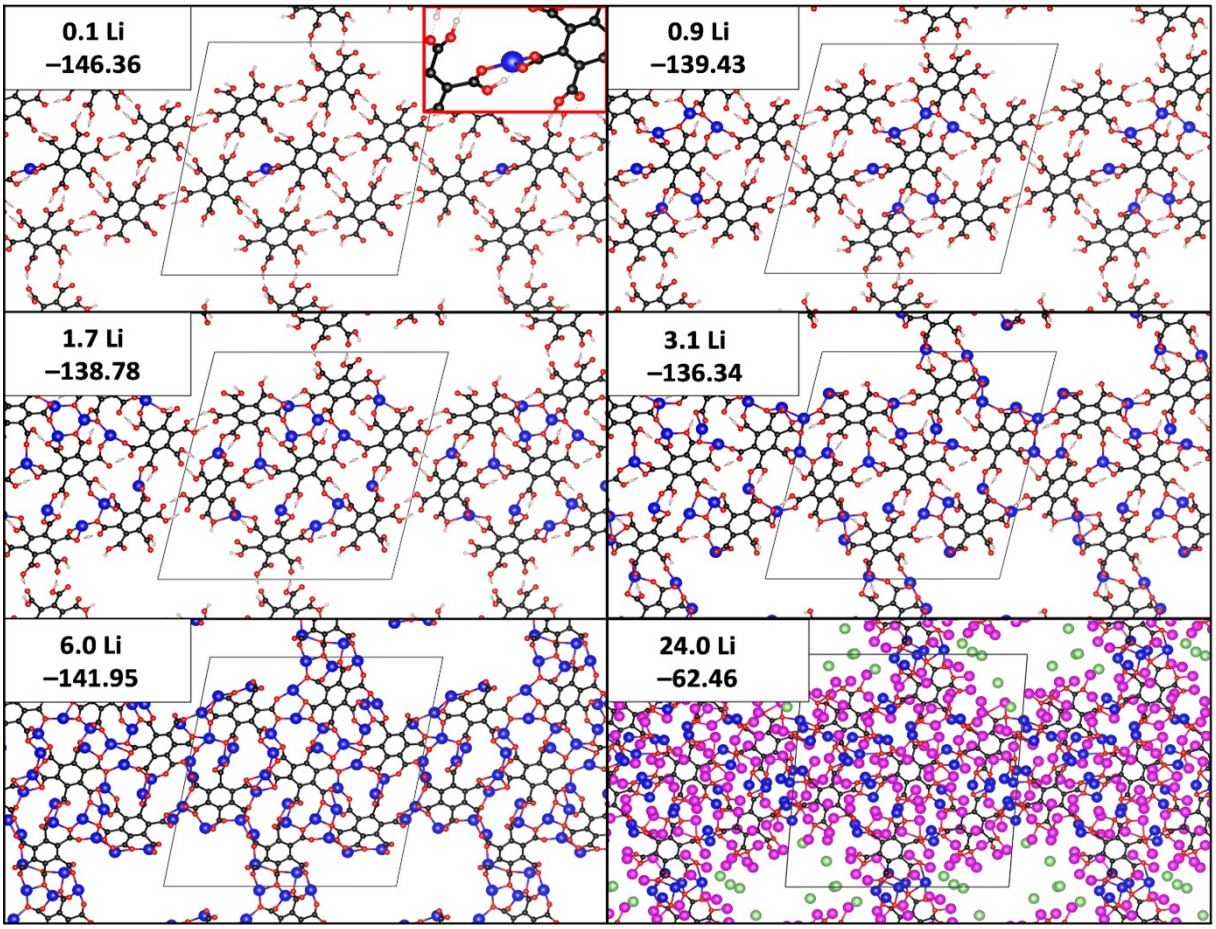

Fig. 20. The bonding of Li atoms to the periodic model of mellitic acid (the gray parallelepiped highlights the supercell). The numbers denote the number of Li atoms per mellitic acid molecule and binding energies per Li atom in kcal mol^{-1}. In the first step, one Li atom was replaced by hydrogen. In the next steps, the number of Li atoms increased up to 24 Li atoms per mellitic acid molecule, corresponding to the maximum loading derived from experiments. The inset depicts the bonding of Li between carboxylic groups. Carbons in black, oxygens in red, hydrogens in white, Li atoms sandwiched between molecules in blue, Li atoms bound to one molecule in magenta, Li atoms without contact with a mellitic acid molecule in green.

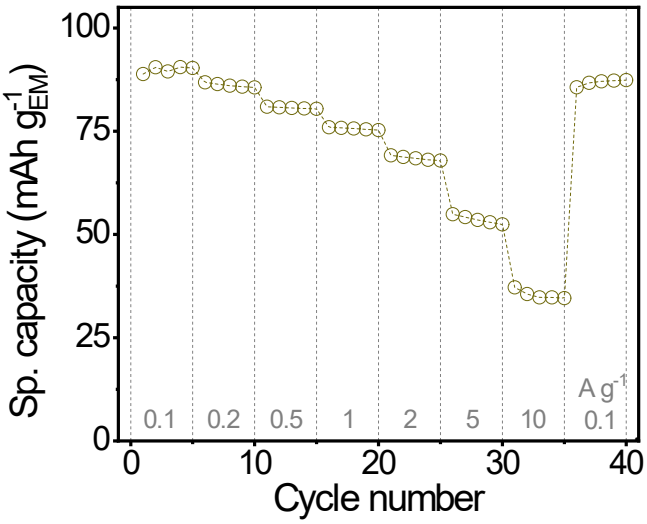

Fig. 21. Galvanostatic current rate test for the calendered PC cathode (PC: CB: PVDF, 90: 3: 7 by mass, m_{EM} = 3.28 mg cm^{-2}) in the 2.0–4.5 V potential range in an PC | Li half-cell. Filled symbols represent discharge capacity.

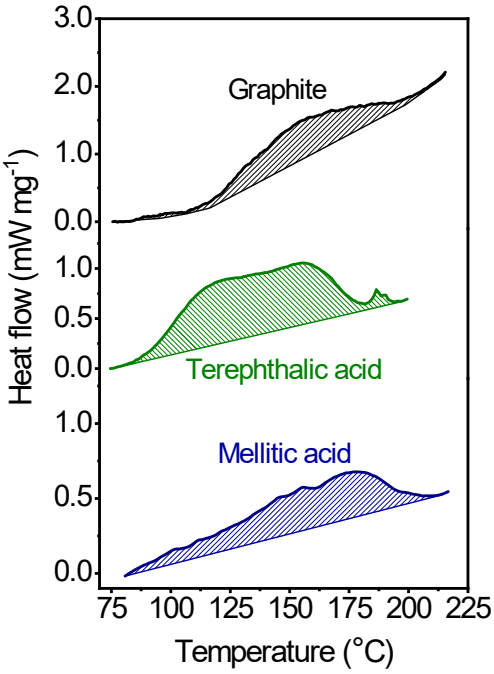

Fig. 22. Differential scanning calorimetry (DSC) measurements of lithiated electrode materials in the presence of electrolytes. The experiments were performed in hermetic Al pans filled with Ar with a 10 °C min^{-1} temperature ramp. The electrodes were after ten charge-discharge cycles followed by lithiation to 0.01 V, electrode material of three MelA-P electrodes was collected for the experiment. The determined heat effect specific to mass or electrode material capacity was −185.7 J g^{-1} or −0.53 J (mAh)$^{-1}$, −256.2 J g^{-1} or −1.58 J (mAh)$^{-1}$, and −125.4 J g^{-1} or −0.12 J (mAh)$^{-1}$ for the graphite, terephthalic acid, and MelA-P electrode materials, respectively.

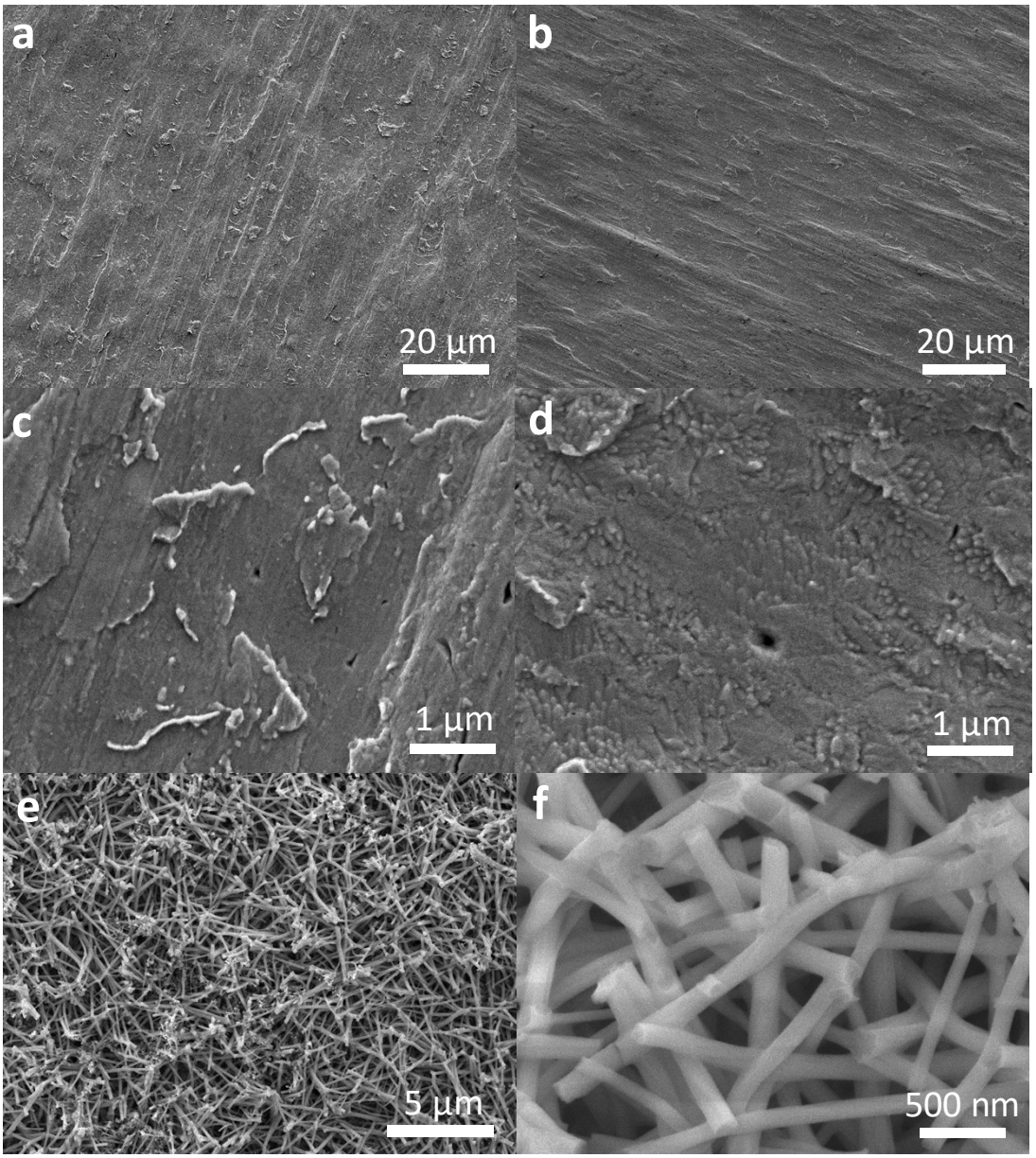

Fig. 23. Scanning electron micrographs of the (a,c) pristine copper foil, (b,d) copper foil exposed to 0.2 M mellitic acid solution for 10 min, followed by washing with ultrapure water, (e,f) MelA-C film on copper foil after washing in ultrapure water for 2 h by shaking (25 min) and ultrasonication (3 min) cycles.

Supplementary Table 1. Comparison of electrochemical properties of MelA with selected reported organic anodes.

Active material	Electrode morphology	Electrode composition, mass loading, and dimensions	Electrolyte and voltage range (V vs. Li)	Q_{AM} (mAh g^{-1}) @ rate (A g^{-1})	Q_{EM}(mAh g^{-1}) @ rate (A g^{-1})	Ref.
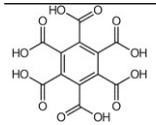 Mellitic acid (MelA)	MelA nanowires ~65 nm average diameter and ~25 µm long nanowires	MelA-P MelA:CB:PANI 50:40:10, 0.8 mg_{EM} cm^{-2} ~34 µm, 1.77 cm^2	1M $LiPF_6$, EC:DMC:EMC, 1:1:1 by mass, 10% FEC 0.01–3.0 V	1888 [a)] @ 0.1 1667 [a)] @ 0.2 1504 [a)] @ 0.5 1310 [a)] @ 1 1108 [a)] @ 2 773 [a)] @ 5 508 [a)] @ 10	1055 @ 0.1 934 @ 0.2 844 @0.5 740 @ 1 630 @ 2 450 @ 5 306 @ 10	**This work**
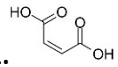 **1.** Maleic acid (MA)	~0.7-µm beads	MA:AB:PVDF, 50:40:10, ~0.35 mg_{EM} cm^{-2} 10 µm, 1.33 cm^2	1 M $LiPF_6$ EC:DMC:DEC, 1:1:1 0.01–3.0 V	~1500 @ 0.0462 ~1028 @ 0.462 ~852 @ 2.31	n.a.	[11] ACS Energy Lett.
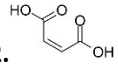 **2.** Maleic acid (MA)	MA@PVDF core-shell 0.5-µm beads with 5–10 nm MA nanocrystals	MA:Super P:PVDF, 50:40:10 1.53 mg_{AM} cm^{-2} AM 43.7 µm, 1.33 cm^2	1 M $LiPF_6$ EC:DEC, 1:1 0.0–3.0 V	1220 @ 0.15 1122 @ 0.3 1120 @ 0.75 1076 @ 1.5 1000 @ 3 815 @ 7.5 644 @ 15 504 @ 30	n.a.	[12] Adv. Energy Mater.
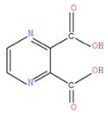 **3.** 2,3-Pyrazinedicarboxylic acid (PZDC)	Unknown	2,3-PZDC:CB:CMC-SBR 50:40:10 0.8 mg_{EM} cm^{-2}, thickness is n.a., 1.33 cm^2	1 M $LiPF_6$ EC:DMC:DEC, 1:1:1 0.01–3.0 V	1155[b)] @ 0.032 1191[b)] @ 0.32	n.a.	[13] J. Power Source
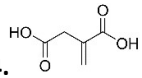 **4.** Itaconic acid (IA)	Foam with 100-nm walls	IA:CB:CMC-SBR 5:4:1 0.4 mg_{AM} cm^{-2} 30 µm, 1.33 cm^2	1 M $LiPF_6$ EC:DMC:DEC, 1:1:1 0.01–3.0 V	1330[b)] @ 0.03 1127[b)] @ 0.3	n.a.	[14] J. Mater. Chem. A

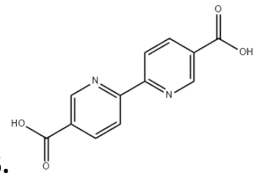 **5.** 2,2-bipyridine-5,5-dicarboxylic acid (H2bpy)	1–10 µm-scale flakes	H2bpy:CB:SBR:CMC 50:40:5:5 ~1 mg_{AM} cm^{-2} 1.33 cm^2	1 M $LiPF_6$ EC:DEC, 1:1 0.01–3.0 V	557 @ 0.08 552 @ 0.12 546 @ 0.2 504 @ 0.4 428 @ 1 308 @ 2	n.a.	[15] Electrochim. Acta
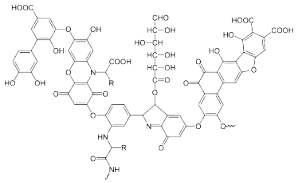 **6.** Humic acid (HA)	~1 µm sheets of varied thickness	Humic acid: CB: PTFE 85:10:5 mass loading is n.a.	1 M $LiPF_6$ EC:EMC:DMC, 1:1:1 0.01–3.0 V	434 @ 0.02 234 @ 0.04 216 @ 0.08 160 @ 0.1 130 @ 0.2 46 @ 0.4	n.a.	[16] Chem. Commun.
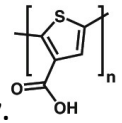 **7.** Carboxylated polythiophene (PTp-COOH)	200-nm nanochunks. Electrochemical performance vanishes with particle size increased to 1 µm	PTp-COOH: CB:PVDF 60:30:10 ~1.0 mg_{AM} cm^{-2}	1 M $LiClO_4$ EC:DEC, 1:1 0.01–3.0 V	743 @0.02 508 @ 0.05 391 @ 0.1 297 @ 0.2 184 @ 0.5 104 @ 1 44 @ 2	n.a.	[17] NPG Asia Mater.
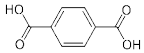 **8.** Terephthalic acid (TA)	~1–2×0.2 µm flakes	TA:CB 70:30 10–12 mg_{EM} per electrode	1 M $LiPF_6$ EC:DMC, 1:1 0.7–3.0 V @ 20°C	300 @ 0.015 (C/20)	n.a.	[18] Nat. Mater.
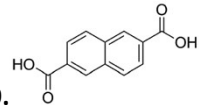 **9.** Sodium naphthalene-2,6-dicarboxylate (SND)	~0.5×1.2×5 µm prismatic microrods	SND:CB:PVDF 60:30:10 1.2–1.5 mg_{AM} cm^{-2}	1 M $LiPF_6$ EC:EMC:DMC, 1:1:1 0.5–3.0 V @ 40 °C	185 @ 0.05 169 @ 0.1 158 @ 0.2 140 @ 0.5 125 @ 1 109 @ 2	n.a.	[19] ACS Appl. Mater. Interfaces

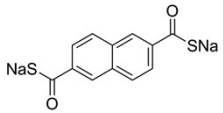 **10.** Sodium naphthalene-2,6-bis(carbothioate) (SNB)	~10 µm stacked nanosheets	SNB:CB:PVDF 60:30:10 1.2–1.5 mg_{AM} cm^{-2}	1 M $LiPF_6$ EC:EMC:DMC, 1:1:1 0.5–3.0 V @ 40 °C	260 @ 0.05 221 @ 0.1 197 @ 0.2 172 @ 0.5 153 @ 1 136 @ 2	n.a.	[19] ACS Appl. Mater. Interfaces
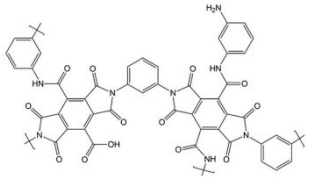 **11** 3D polyimide-based NPs/Ni nanofoam (3D PIN/Ni)	Ti/photopolymer/Ni-templated nanofoam with ~100-nm channels current collector	AM was synthesized over 3D Ni nanofoam ~0.3 cm^2, 6.3 µm with the collector foam. The EM mass loading is n.a.	1 M $LiPF_6$ EC:DMC, 1:1 0.01–3.0 V	1365 @ 1.5 903 @ 15 696 @ 30 438 @ 120 276 @ 300 185 @ 600	n.a.	[20] Energy Environ. Sci.
Polyimide-based NPs (PIN)	n.a.	PIN:CB:PTFE 40:40:10 free standing film mass loading is n.a.	1 M $LiPF_6$ EC:DMC, 1:1 0.01–3.0 V	259 @ 1.5	n.a.	[20] Energy Environ. Sci.
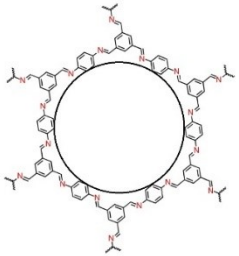 **12.** Imine-based COF over SWCNTs CNTs (COF@CNTs)	5-nm COF layer over SWCNTs, few-µm scale agglomerates	(COF@CNTs):AB:PVDF 8:2:1 2 mg_{EM} cm^{-2}, 20 µm electrode area is n.a.	1 M $LiPF_6$ EC:DEC, 1:1 0.05–3.0 V	**COF@CNTs** 1021 @ 0.1 874 @ 0.2 633 @ 0.5 470 @ 1 336 @ 2 217 @ 5 **Bulk COF** 217 @ 0.1 **COF in COF@CNTs** 1536 @ 0.1	n.a.	[21] Nat. Commun.

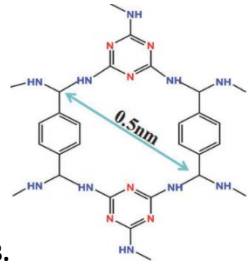 **13.** Exfoliated Triazine-Based (E-SNW-1/CNT)	0.01–1 µm COF nanosheets and SWCNTs	E-SNW-1/CNTs: Super P: PVDF 8:1:1 ~1.5 mg_{EM} cm^{-2}, 20 µm electrode area is n.a. COF:CNTs is ~2:1	1 M $LiPF_6$ EC:DEC, 1:1 0.001–3.0 V	**E-SNW-1/CNTs** 584 @ 0.1 500 @ 0.2 418 @ 0.5 370 @ 1 302 @ 2 214 @ 5 **E-SNW-1 in E-SNW-1/CNTs** 920 @ 0.1	n.a.	[22] Adv. Energy Mater.
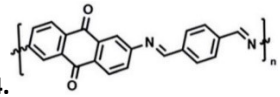 **14.** Poly(imine-anthraquinone)	0.3–1.0 µm flakes	PIAQ:KB:CMC 7:2:1 ~1.4–1.9 mg_{AM} cm^{-2} 0.64 cm^2, 8×8 mm electrode thickness is n.a.	1 M $LiPF_6$ EC:DEC, 1:1 0.01–3.5 V	1291 @ 0.1 891 @ 0.2 653 @ 0.5 390 @ 1 224 @ 2	n.a.	[23] J. Mater. Chem. A
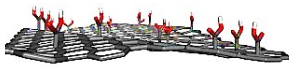 **15.** Graphene acid	~5 µm flakes	GA:CB:PVDF 90:5:5 1.0–1.5 mg cm^{-2}, 20 µm 1.77 cm^2	1 M $LiPF_6$ EC:DMC, 1:1 0.01–3.0 V	721[a)] @ 0.05 493[a)] @ 0.1 374[a)] @ 0.2 272[a)] @ 0.5 214[a)] @ 1 188[a)] @ 1.5 172[a)] @ 2	700 @ 0.05 488 @ 0.1 375 @ 0.2 275 @ 0.5 217 @ 1 190 @ 1.5 174 @ 2	[24] Adv. Energy Mater.

CB - carbon black; EM - electrode material; PANI – polyaniline (emeraldine base); PVDF - polyvinylidene fluoride; CMC - carboxymethyl cellulose; SBR - styrene-butadiene rubber, n.a. stands for “not available.

[a)] AM capacity values were recalculated from EM capacity according to the Supplementary Note 1 using capacity of CB determined at different current rates.

[b)] The stabilized capacity for a symmetrical charge-discharge current was used for comparison.

Supplementary Table 2. The list of comparative samples and the highlights of the results. Capacity here is reported with respect to the whole mass of the electrode material (EM).

#	Material	Purpose	Composition, mass%	Morphology	Comment	Capacity mAh g_{EM}^{-1} @ A g^{-1}
1	Pure MelA	Effect of CB	100	Macroscale dendrites		16 @ 0.1
2	MelA:CB	Effect of CB	95:5	Concentric dendrites		48 @ 0.1
3	MelA:CB	Effect of CB	90:10	Concentric dendrites	Cell failed during OCP	n.a.
4	MelA:CB	Effect of CB	80:20	Flat, uniform	Pealing-off film	n.a.
5	MelA:CB	Effect of CB	70:30	Nanowires	Pealing-off film	n.a.
6	MelA:CB	Effect of CB	60:40	Nanowires	cracked film	856 @ 0.1
7	**MelA-C (MelA:CB)**	Effect of PANI	50:50	Nanowires	Stable film	777 @ 0.1
8	MelA-C-Ti (MelA:CB)	Effect of Cu	50:50	Nanoparticles	Cast over Ti substrate	124 @ 0.1
9	**MelA-P (MelA:CB:PANI)**	EM optimization	50:40:10	**Nanowires**	**Stable film**	**1055 @ 0.1**
10	MelA:CB:PANI	EM optimization	50:30:20	Nanowires		940 @ 0.1
11	MelA:CB:PANI	EM optimization	50:45:5	Nanowires		862 @ 0.1
12	MelA:CB:PANI	EM optimization	53:40:7	Nanowires		858 @ 0.1
13	MelA-P-hot (MelA:CB:PANI)	Nanomorphology	50:40:10	Nanoparticles	Cast at 60 °C	727 @ 0.1
14	MelA-P-NMP (MelA:CB:PANI)	Nanomorphology	50:40:10	Nanoparticles	NMP-based slurry	33 @ 0.1
15	Terephthalic acid (TA:CB:PANI)	Comparison	50:40:10	n.a.	NMP-based slurry	110 @ 0.1
16	Trimesic acid (TrA:CB:PANI)	Comparison	50:40:10	n.a.	NMP-based slurry	122 @ 0.1
17	CB:PVDF	Contribution of CB	70:30	n.a.		194 @ 0.1
18	PANI:CB	Contribution of PANI	50:50	n.a.		123 @ 0.1

Supplementary Table 3. EIS fitting parameters for MelA-P nanorod anode.

State of the cell	R_S (Ω)	R_{CT} (Ω)	Q_{DL} m(F.s$^{(n-1)}$)	n_{DL}	Q_{LF} m(F.s$^{(n-1)}$)	n_{LF}	$W_{diff.}$ (Ω)	$t_{diffusion}$ (s)
As assembled	2.0	124	3.24×10^{-5}	0.825	1.98×10^{-3}	0.851	2.24×10^{-3}	10^{-5}
After 3@0.05	3.3	12.9	0.699	0.965	0.533	0.554	8.302	2.1×10^{-3}
After 10@0.2	4.2	9.2	4.932	0.456	1.406	0.699	1.939	1.3×10^{-4}
After 50 @0.2	5.2	2.8	1.686	0.595	0.0626	0.848	1.555	0.1778
After 100 @0.2	6.5	1.6	1.755	0.645	0.0564	0.868	12.06	15.49

Supplementary Table 4. Performance comparison of high-energy supercapacitors. Specific energy and power were taken for the last cycle of each current rate and normalized to the total mass of electrode materials where necessary.

Device configuration	Cell voltage (V)	Max. specific energy (Wh kg^{-1} $_{EM\ total}$)	Max. specific power (kW kg^{-1} $_{EM\ total}$)	Ref.
Mellitic acid|PC	2.0–4.5	155.9 @ 0.34 kW kg^{-1}	19.4 @ 60.2 Wh kg^{-1}	This work
Maleic acid|Kuraray [a]	0.0–4.3	124.5 @ 0.042 kW kg^{-1}	4.51 @ 55.7 Wh kg^{-1}	[12] *Adv. Energy Mater.*
SnS_2-rGO|BNC[b]	0.0–4.5	125.2 @ 0.074 kW kg^{-1}	29.2 @ 50.5 Wh kg^{-1}	[25] *Adv. Energy Mater*.
0D-T-Nb_2O_5-C|PN-C[c]	0.05–3.0	80.9 @ 0.11 kW kg^{-1}	6.07 @ 64.9 Wh kg^{-1}	[26] *Nano Energy*
PHATN|$Ni(OH)_2$[d]	0.0–1.1	52 @ 0.480 kW kg^{-1}	8.0 @ 17.8 Wh kg^{-1}	[27] *Nat. Mater.*
Gr|Li_2DHBN-AC[d]	2.2–4.0	54.9 @ 0.05 kW kg^{-1}	2.8 @ 22.1 Wh kg^{-1}	[28] *Nat. Mater.*
Zr-MOF|AC[b]	1.0–4.0	~98 @ 0.21 kW kg^{-1}	~10.5 @ 30 Wh kg^{-1}	[29] *Small*

[a] E_{sp} was normalized to the total mass of EM on the cathode and the anode in the given mass ratio and EM commpositions; P_{sp} was recalculated for the normalized E_{sp} by the authors' method.

[b] P_{sp} was normalized to the total mass of EM on the cathode and the anode in the given mass ratio and EM commpositions; E_{sp} was recalculated for the normalized P_{sp} by the authors' method.

[c] Only E_{sp} was normalized to the total mass of EM on the cathode and the anode.

[d] E_{sp} and P_{sp} were taken as they are reported by authors.

Supplementary references:

1. Kresse, G. & Hafner, J. Ab initio molecular dynamics for liquid metals. *Phys. Rev. B* **47**, 558–561 (1993).
2. Kresse, G. & Furthmüller, J. Efficiency of ab-initio total energy calculations for metals and semiconductors using a plane-wave basis set. *Comput. Mater. Sci.* **6**, 15–50 (1996).
3. Kresse, G. & Furthmüller, J. Efficient iterative schemes for ab initio total-energy calculations using a plane-wave basis set. *Phys. Rev. B* **54**, 11169–11186 (1996).
4. Blöchl, P. E. Projector augmented-wave method. *Phys. Rev. B* **50**, 17953–17979 (1994).
5. Kresse, G. & Joubert, D. From ultrasoft pseudopotentials to the projector augmented-wave method. *Phys. Rev. B* **59**, 1758–1775 (1999).
6. Perdew, J. P., Burke, K. & Ernzerhof, M. Generalized Gradient Approximation Made Simple. *Phys. Rev. Lett.* **77**, 3865–3868 (1996).
7. Grimme, S. Semiempirical GGA-type density functional constructed with a long-range dispersion correction. *J. Comput. Chem.* **27**, 1787–1799 (2006).
8. Forghani, M. & Donne, S. W. Method Comparison for Deconvoluting Capacitive and Pseudo-Capacitive Contributions to Electrochemical Capacitor Electrode Behavior. *J. Electrochem. Soc.* **165**, A664 (2018).
9. Wen, C. J., Boukamp, B. A., Huggins, R. A. & Weppner, W. Thermodynamic and Mass Transport Properties of " LiAl ". *J. Electrochem. Soc.* **126**, 2258 (1979).
10. Weppner, W. & Huggins, R. A. Determination of the Kinetic Parameters of Mixed-Conducting Electrodes and Application to the System Li3Sb. *J. Electrochem. Soc.* **124**, 1569 (1977).
11. Wang, Y. *et al.* Ultrahigh-Capacity Organic Anode with High-Rate Capability and Long Cycle Life for Lithium-Ion Batteries. *ACS Energy Lett.* **2**, 2140–2148 (2017).

12. Hu, Z. *et al.* Self-Assembled Binary Organic Granules with Multiple Lithium Uptake Mechanisms toward High-Energy Flexible Lithium-Ion Hybrid Supercapacitors. *Adv. Energy Mater.* **8**, 1802273 (2018).

13. Wang, Y. *et al.* The effect of carboxyl group position of pyrazinedicarboxylic acid on electrochemical performances in lithium ion batteries anode. *J. Power Sources* **473**, 228515 (2020).

14. Wang, Y. *et al.* A high-capacity organic anode with self-assembled morphological transformation for green lithium-ion batteries. *J. Mater. Chem. A* **7**, 22621–22630 (2019).

15. Bo, Y. *et al.* Bipyridine carboxylic acid as a high-performance anode material for lithium- and sodium-ion batteries. *Electrochimica Acta* **405**, 139628 (2022).

16. Zhu, H., Yin, J., Zhao, X., Wang, C. & Yang, X. Humic acid as promising organic anodes for lithium/sodium ion batteries. *Chem. Commun.* **51**, 14708–14711 (2015).

17. Numazawa, H., Sato, K., Imai, H. & Oaki, Y. Multistage redox reactions of conductive-polymer nanostructures with lithium ions: potential for high-performance organic anodes. *NPG Asia Mater.* **10**, 397–405 (2018).

18. Armand, M. *et al.* Conjugated dicarboxylate anodes for Li-ion batteries. *Nat. Mater.* **8**, 120–125 (2009).

19. Wang, J. *et al.* Three-Electron Redox Enabled Dithiocarboxylate Electrode for Superior Lithium Storage Performance. *ACS Appl. Mater. Interfaces* **10**, 35469–35476 (2018).

20. Ham, Y. *et al.* 3D periodic polyimide nano-networks for ultrahigh-rate and sustainable energy storage. *Energy Environ. Sci.* **14**, 5894–5902 (2021).

21. Lei, Z. *et al.* Boosting lithium storage in covalent organic framework via activation of 14-electron redox chemistry. *Nat. Commun.* **9**, 576 (2018).

22. Lei, Z., Chen, X., Sun, W., Zhang, Y. & Wang, Y. Exfoliated Triazine-Based Covalent Organic Nanosheets with Multielectron Redox for High-Performance Lithium Organic Batteries. *Adv. Energy Mater.* **9**, 1801010 (2019).

23. Man, Z. *et al.* High-performance lithium–organic batteries by achieving 16 lithium storage in poly(imine-anthraquinone). *J. Mater. Chem. A* **7**, 2368–2375 (2019).

24. Obraztsov, I. *et al.* Graphene Acid for Lithium-Ion Batteries—Carboxylation Boosts Storage Capacity in Graphene. *Adv. Energy Mater.* **12**, 2103010 (2022).

25. Hao, Y., Wang, S., Shao, Y., Wu, Y. & Miao, S. High-Energy Density Li-Ion Capacitor with Layered SnS2/Reduced Graphene Oxide Anode and BCN Nanosheet Cathode. *Adv. Energy Mater.* **10**, 1902836 (2020).

26. Hemmati, S. *et al.* 3D N-doped hybrid architectures assembled from 0D T-Nb2O5 embedded in carbon microtubes toward high-rate Li-ion capacitors. *Nano Energy* **56**, 118–126 (2019).

27. Russell, J. C. *et al.* High-performance organic pseudocapacitors via molecular contortion. *Nat. Mater.* **20**, 1136–1141 (2021).

28. Jeżowski, P. *et al.* Safe and recyclable lithium-ion capacitors using sacrificial organic lithium salt. *Nat. Mater.* **17**, 167–173 (2018).

29. Yan, W. *et al.* High-Performance Lithium-Ion Capacitors Based on Porosity-Regulated Zirconium Metal−Organic Frameworks. *Small* **17**, 2005209 (2021).